Check for updates

ASME Journal of Manufacturing Science and Engineering
Online journal at:
https://asmedigitalcollection.asme.org/manufacturingscience

Alex Riensche[1]
Sooner Advanced Manufacturing Laboratory,
University of Oklahoma,
Norman, OK 73069;
Grado Department of Industrial and Systems Engineering,
Virginia Tech,
Blacksburg, VA 24061
e-mail: ariensche@ou.edu

Kaustubh Deshmukh
Department of Mechanical Engineering,
Virginia Tech,
Blacksburg, VA 24061
e-mail: kd15@vt.edu

Antonio Carrington Jr.
Grado Department of Industrial and Systems Engineering,
Virginia Tech,
Blacksburg, VA 24061
e-mail: arcarringtonjr@vt.edu

Mihir Darji
Grado Department of Industrial and Systems Engineering,
Virginia Tech,
Blacksburg, VA 24061
e-mail: mihir2560@vt.edu

Benjamin Bevans
Sooner Advanced Manufacturing Laboratory,
University of Oklahoma,
Norman, OK 73069;
Grado Department of Industrial and Systems Engineering,
Virginia Tech,
Blacksburg, VA 24061
e-mail: benjamin.bevans@ou.edu

Kyle Snyder
Commonwealth Center for Advanced Manufacturing,
Disputanta, VA 23842
e-mail: kyle.snyder@ccam-va.com

John Sions
Commonwealth Center for Advanced Manufacturing,
Disputanta, VA 23842
e-mail: john.sions@ccam-va.com

Rapid, Autonomous, and Shape-Agnostic Physics-Guided Thermal History Control to Improve Part Quality in Laser Powder Bed Fusion Additive Manufacturing

This work concerns the laser powder bed fusion (LPBF) additive manufacturing process. We developed and implemented a physics-based approach for layerwise control of the thermal history of an LPBF part. Controlling the thermal history of an LPBF part during the process is crucial as it influences critical-to-quality characteristics, such as porosity, solidified microstructure, cracking, surface finish, and geometric integrity, among others. Typically, LPBF processing parameters are optimized through exhaustive empirical build-and-test procedures. However, because thermal history varies with geometry, processing parameters seldom transfer between different part shapes. Furthermore, particularly in complex parts, the thermal history can vary significantly between layers leading to both within-part and between-part variation in properties. In this work, we devised an autonomous physics-based controller to maintain the thermal history within a desired window by optimizing the processing parameters layer by layer. This approach is a form of digital feedforward model predictive control. To demonstrate the approach, five thermal history control strategies were tested on four unique part geometries (20 total parts) made from stainless steel 316L alloy. The layerwise control of the thermal history significantly reduced variations in grain size and improved geometric accuracy and surface finish. This work provides a pathway for rapid, shape-agnostic qualification of LPBF part quality through control of the causal thermal history as opposed to expensive and cumbersome trial-and-error parameter optimization.
[DOI: 10.1115/1.4068695]

Keywords: laser powder bed fusion, qualification, thermal history control, model predictive control, feedforward control, additive manufacturing, inspection and quality control, modeling and simulation, process engineering, sensors, Inconel 718, microstructure, surface finish, geometric integrity, meltpool, primary dendritic arm spacing

Downloaded from http://asmedigitalcollection.asme.org/manufacturingscience/article-pdf/147/8/081005/7500901/manu-25-1025.pdf by Virginia Polytechnic Institute and State University user on 27 June 2025

[1]Corresponding author.
Manuscript received January 9, 2025; final manuscript received April 14, 2025; published online June 5, 2025. Assoc. Editor: Arif S Malik.

Copyright © 2025 by ASME

Yuri Plotnikov
Commonwealth Center for Advanced Manufacturing,
Disputanta, VA 23842
e-mail: yuri.plotnikov@ccam-va.com

Kevin D. Cole
Mechanical and Materials Engineering,
University of Nebraska-Lincoln,
Lincoln, NE 68588
e-mail: kcole1@unl.edu

Prahalada Rao
Grado Department of Industrial and Systems Engineering;
Department of Mechanical Engineering,
Virginia Tech,
Blacksburg, VA 24061
e-mail: prahalad.k.rao@vt.edu

Downloaded from http://asmedigitalcollection.asme.org/manufacturingscience/article-pdf/147/8/081005/7500901/manu-25-1025.pdf by Virginia Polytechnic Institute and State University user on 27 June 2025

1. Introduction

1.1 Objective and Motivation. In this work, we developed and applied a physics-guided model predictive control approach to regulate the thermal history and thereby improve the functional integrity of laser powder bed fusion (LPBF)-processed parts. We test and affirm the hypothesis that layerwise control of the thermal history mitigates variation in critical-to-quality characteristics such as grain size, geometric integrity, and surface finish [1–3]. The key idea is to control the thermal history of the part within a desired window. This is achieved by adjusting the processing parameters between layers guided by predictions from a physics-based computational thermal model. The approach produces a layerwise processing plan for each part contingent on its geometry and the desired thermal history trend before printing commences—a form of digital feedforward model predictive process control.

In the LPBF process, as shown in Fig. 1, material is deposited onto a build plate by a recoater balde or roller in layers that are 20–60 μm in thickness. Subsequently, an infrared (IR) laser (200–500 W) is rapidly scanned on the surface (500–1000 mm/s) via a galvanometric mirror assembly to melt the deposited layer of material [2,3]. The process is capable of producing complex parts from alloys of iron, titanium, nickel, among others [4].

The LPBF process is advantageous for manufacturing complex, high-value components that are difficult to create with subtractive and formative methods. Industry case studies show that LPBF enables a significant reduction in manufacturing lead times and intermediate steps [5,6]. For example, NASA recently demonstrated that LPBF-manufactured rocket engine combustion chamber liners made from a new copper–chromium–niobium alloy achieved over 60% cost saving and threefold reduction in lead time relative to those produced using conventional subtractive manufacturing [7,8]. In a similar vein, the production of titanium aluminide low-pressure turbine blades for the GE9X turbofan engine resulted in a 50% reduction in weight compared to cast nickel alloy turbine blades, which in turn reduced fuel consumption by 10% [9].

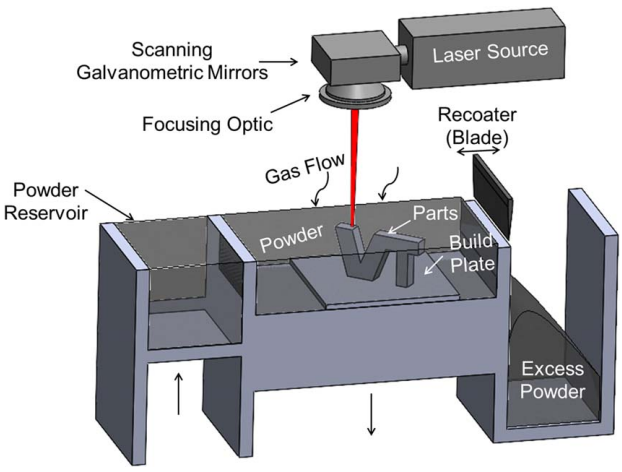

Fig. 1 A schematic diagram of the LPBF process

Despite these abilities and advantages, the adoption of LPBF in safety-critical industries is currently limited due to the lack of consistency between parts [10]. In addition, variation occurs within the same part in terms of microstructure evolution, flaw formation, and part properties [11–13]. To explain further, the spatiotemporal distribution of temperature in an LPBF part as it is being printed, commonly termed thermal history, has a significant influence on critical-to-quality characteristics, such as porosity, microstructure evolution, cracking, surface finish, geometric integrity, among others [14,15]. The thermal history is a function of material properties, part geometry, and processing parameters [16–18]. Currently, the optimal processing parameters that prevent flaw formation in LPBF parts are ascertained through extensive empirical studies without regard for the thermal history [4]. Simple shapes such as cubes, cylinders, and tensile coupons are built under varying processing parameters, typically using the statistical design of experiments [19,20]. Part characteristics are subsequently ascertained postprocess using such techniques as optical and scanning electron microscopy (SEM) and X-ray computed tomography [20,21]. Extensive mechanical testing is further conducted to determine physical properties, e.g., strength and fatigue [22,23]. Once the optimal processing conditions are identified, they are tested on practical parts. However, these empirically optimized processing conditions seldom transfer successfully to complex geometries, necessitating further rounds of experiments [24]. It is estimated that such empirical-guided process optimization, metallurgical analysis, and mechanical testing of samples require over 4 years and can cost several million dollars [4,25].

To explain further, despite process optimization, there may be significant variation in the microstructure evolved between two different part geometries of the same material printed under identical processing conditions. Indeed, apart from processing parameters, build layout-related factors such as part orientation, presence (or absence) of other parts on the build plate, and placement of supports influence the thermal history [20,26,27]. Researchers have reported

that a relatively small deviation in the build conditions, e.g., changing the dwell time between layers (TBLs), adding or removing parts from a build plate, can result in significant changes in the properties of a previously qualified part [27]. Hence, besides being prohibitively expensive to obtain, the empirically optimized parameters are specific to a part design and build layout [28]. Once optimized, the current practice is to maintain the processing parameters constant during printing of the bulk part volume, albeit empirically determined modifications are made while scanning the part boundary and certain features, such as overhangs. Since the cross-sectional area of the part varies between layers, the time between layers is not constant, which in turn causes a nonuniform temperature distribution. The spatiotemporal variation in the temperature distribution engenders prominent differences in the microstructure within the same part [29]. The large within-part variation in microstructure resulting from an uneven temperature distribution is exemplified in Fig. 2, which shows two identical 20 mm tall LPBF-produced Inconel 718 parts processed under different laser power (P) conditions on the same build plate [30]. The rest of the processing conditions were identical. Thermal simulations published in our previous work predicted that the overhang regions of these parts tend to overheat [30]. This inhomogeneous thermal distribution causes anisotropy in the grain size (primary dendritic arm spacing (PDAS)), microstructure type, and direction of grain growth, as evident in the scanning electron microscopy images.

The image shown in Fig. 2(*a*) is processed at laser power $P = 200$ W. The PDAS near the top of the part is ~700 nm, while the PDAS near the mid-section is ~600 nm. These differences in the evolved microstructure within the same part result from the uneven temperature distribution between layers [30]. The uneven temperature distribution between layers is further magnified in Fig. 2(*b*) when using a higher laser power of $P = 370$ W, with all other conditions maintained constant. The higher laser power condition exacerbates heat retention and leads to high-temperature gradients between layers. The increased heat retention results in larger PDAS at the top (~900 nm) compared to the mid-section (~700 nm). Therefore, to obtain consistent microstructure within a part, as well as between parts, it is essential to control the thermal history layer by layer [3]. In other words, processing parts under fixed parameters without considering the effect of part shape on thermal history is liable to result in inconsistent properties.

1.2 Approach, Novelty, and Limitations. This work presents a physics-based approach to mitigate within-part variation and curtail costly build-and-test optimization in LPBF. The approach, summarized in Fig. 3, is based on a concept called feedforward model predictive control. The approach autonomously optimizes the processing parameters layer by layer before the part is printed to maintain the thermal history within an *a priori* defined target window [31,32]. The main principle is to iteratively simulate the thermal history as a function of different processing parameters, until the predicted thermal history matches a predetermined ideal or target thermal history. Thus, instead of maintaining the processing parameters constant during the printing of a part, the approach creates a dynamic processing plan with parameters that change between layers.

Since the underlying computational thermal simulation accounts for the shape of a part, the model-derived processing plan is unique for every part geometry. Further, the simulation considers the effect of build condition-related factors, such as other parts on the build plate, time between layers, among others [18,33]. To the best of our knowledge, this is one of the first works to develop and implement a part-level, physics-guided digital feedforward process control approach in LPBF—a significant departure from existing empirical and heuristic process adjustment approaches [34,35].

The model predictive control approach consists of four steps as summarized in Fig. 3. These steps are labeled as follows: (1) predict, (2) identify, (3) parse, and (4) select. Steps 3 and 4 are iterative in nature. These steps are briefly summarized herewith in the context of a cone-shaped part studied in this work and will be discussed in detail in Sec. 4.

- Step 1 (Predict): The thermal history of a part is predicted using a rapid and meshless, graph theory-based thermal simulation model developed in our previous works [30,33,36]. The inputs to the model are the part geometry, orientation, materials properties, processing conditions suggested by the manufacturer, time between layers, and heat transfer boundary conditions. This is the nominal or default thermal history under constant processing conditions, i.e., the thermal history is not controlled. The predicted thermal history for this uncontrolled condition is demarcated as $\hat{T}_{\text{orginal}}$. In Fig. 3, $\hat{T}_{\text{orginal}}$ for the cone-shaped part depicts potentially deleterious heat accumulation and large variation in temperature between layers.
- Step 2 (Identify): An ideal or target thermal history ($\hat{T}_{\text{ideal}}$) is selected to overcome the deleterious thermal history trends identified in $\hat{T}_{\text{orginal}}$ for the uncontrolled condition in step 1. In this work, four different strategies for selecting the ideal thermal history were evaluated.
- Step 3 (Parse): The thermal history of the part is predicted as a function of various processing parameter levels ($\hat{T}_P$). Essentially, a simulation-driven grid search is conducted over a set of candidate processing parameters. In this work, the laser power levels are varied within constraints motivated from practice. The laser power is constrained to five discrete

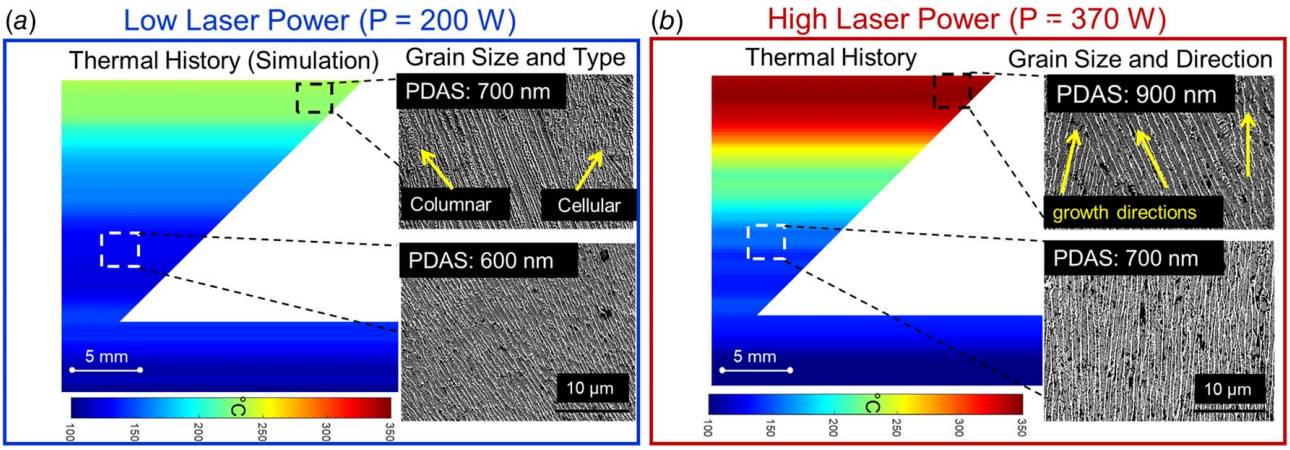

Fig. 2 Uneven thermal distribution causes anisotropy in the microstructure within the same LPBF part [30]. The parts are 20 mm tall (Inconel 718).

Downloaded from http://asmedigitalcollection.asme.org/manufacturingscience/article-pdf/147/8/081005/7500901/manu-25-1025.pdf by Virginia Polytechnic Institute and State University user on 27 June 2025

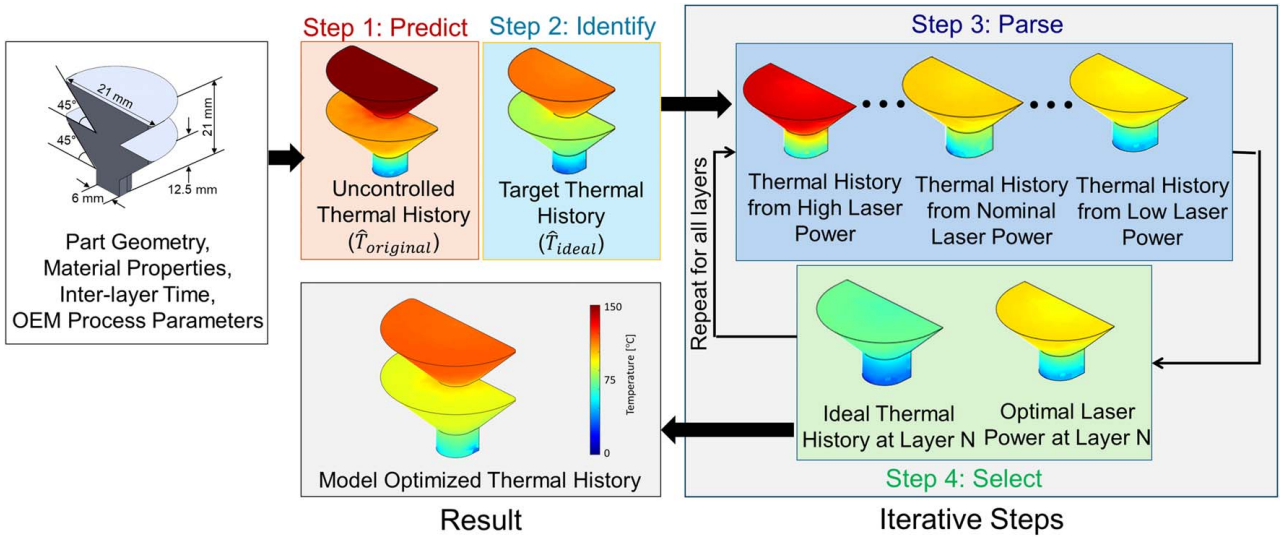

Fig. 3 Overview of the model predictive control approach. Shown here is an example of the cone geometry studied in this work. The approach has four steps: (1) predict, (2) identify, (3) parse, and (4) select. Steps 3 and 4 are iterative. The thermal history shown here is the end-of-cycle temperature at discrete epochs.

levels between 180 W and 245 W, to avoid keyhole porosity and lack of fusion, respectively, in stainless steel 316L [17,37].

- Step 4 (Select): The algorithm picks the processing parameters from Step 3 that result in the closest match (minimum absolute deviation) of the predicted thermal history ($\hat{T}_P$) with the corresponding layers for the ideal thermal history ($\hat{T}_{\text{ideal}}$) from step 2.

Steps 3 and 4 are repeated iteratively at intervals of two layers. The outcome is a layer-by-layer process plan that minimizes deviations of the actual thermal history ($\hat{T}_P$) from the ideal or desired thermal history ($\hat{T}_{\text{ideal}}$). However, as depicted in Fig. 3, it is not possible in practice for the final optimized thermal history to match exactly the ideal thermal history because the adjustable levels of laser power were constrained between 180 W and 245 W.

Existing finite element (FE) thermal modeling techniques are computationally cumbersome [38–40]. Therefore, the iterative simulation of the thermal history in steps 3 and 4 inherent to model predictive control is not amenable to FE modeling. To overcome this impediment, we used a meshless, semianalytical graph theory-based approach, which has been shown in prior works to be an order of magnitude faster than FE-based thermal modeling [36,41]. For the 21 mm tall cone-shaped part exemplified in Fig. 3, the control algorithm autonomously produced a process parameter plan within 4 h, and one iteration required less than 7 min. By contrast, existing FE-based models would require significantly more time to converge for one iteration of an entire part [40]. Although commercial FE-based solutions for thermal modeling can drastically reduce the computation time compared to research-level FE solutions, they do not currently incorporate the ability to autonomously prescribe adjustment of parameters [42].

A limitation of the model predictive control approach implemented in this work is that only one processing parameter, the laser power (P), was adjusted between five discrete levels. While multiple process input variables, such as the laser velocity, hatch spacing, and layer height, could be adjusted within the graph theory computational thermal model, these other parameters were avoided due to the high computational expense for conducting a multiparameter grid search in step 3. Moreover, adjusting certain processing parameters might not be conducive to process stability. To explain further, the input energy density ($E_V = \frac{P}{V \cdot H \cdot L}$ (J/m^3)) can be controlled as a function of four processing parameters, namely, laser power (P (W)), laser velocity (V (m/s)), hatch spacing (H (m)), and layer height (L (m)) [43,44]. Increasing V to decrease E_V for avoiding heat retention in the part is liable to create meltpool instability and spatter [37]. Changing L requires mechanical repositioning of the powder bed adding to processing time. Lastly, increasing H to decrease E_V may potentially cause poor consolidation of tracks within a layer, resulting in lack-of-fusion porosity [44]. Another limitation in the current work is that it does not evaluate residual stresses and mechanical properties owing to the relatively complex geometries of the parts tested.

1.2.1 Differences From Authors' Prior Works. In a previous publication, we implemented a feedforward control approach for LPBF, which involved adjusting laser power and interlayer dwell time between layers [41]. This prior work demonstrated that modifying laser power and increasing dwell time to mitigate heat accumulation resulted in consistent microstructure and improved geometric resolution compared to parts built under constant processing conditions. However, this approach had a significant limitation that is addressed by the model predictive control approach presented in the current work. Our prior work lacked a target or ideal thermal history, and in other words, there was no "Identify Step 2" in Fig. 3. The goal was merely to mitigate large-scale heat buildup-based and trial-and-error computer simulations. This previous heuristic feedforward approach could not control the thermal history to a specific desired trend. In contrast, the current approach autonomously adjusts the process parameters so that the thermal history is maintained with a desired window. Another key difference from the previous work concerns the various aspects of thermal history that are controlled. As will be explained in depth in Sec. 4.4, in this work, four thermal history control strategies are tested, ranging from control of end-of-cycle temperature, layerwise temperature gradient, cooling rate, and interlayer time (ILT). The previous work was restricted to control of end-of-cycle temperature. In another of our recent works, we demonstrated the concept of model predictive control of thermal history in LPBF [45]. However, in the foregoing work, only one thermal control strategy was tested, i.e., control of end-of-cycle temperature [45].

The rest of this article is organized as follows. In Sec. 2, we briefly review the existing literature and identify the gaps in the state of the art in process control in LPBF. Section 3 describes the experimental setup, build plan, exemplar parts studied, and methods for their characterization. Discussed in Sec. 4 is the development of the model predictive process control approach, proposition of various thermal control strategies, and calibration and validation of the graph theory thermal model. The results from

Downloaded from http://asmedigitalcollection.asme.org/manufacturingscience/article-pdf/147/8/081005/7500901/manu-25-1025.pdf by Virginia Polytechnic Institute and State University user on 27 June 2025

applying model predictive control to four different exemplar parts are reported in Sec. 5. Finally, summarized in Sec. 6 are conclusions and avenues for further research.

2 Prior Work in Process Control in LPBF

Process control, as outlined in Fig. 4, can be segmented into two broad approaches, namely, closed-loop feedback control and open-loop feedforward control [46,47]. The application of these process control approaches to LPBF is discussed herewith.

2.1 Closed-Loop Feedback Process Control. Closed-loop control incorporates feedback from sensor(s) that measure the output variable(s) of the process $y(t)$ that needs to be controlled. Based on the sensor data, the controller assesses the process drift from a desired setpoint or target $r(t)$ in terms of the error signal $e(t) = r(t) - y(t)$. Depending on $e(t)$, the controller produces a control signal $u(t)$ to adjust the process parameters and return the output $y(t)$ to the desired setpoint $r(t)$. The controller can be based on a mathematical model or heuristic (empirical) algorithm. For example, proportional–integral–derivative (PID) is a popular feedback control approach that considers the magnitude, cumulative, and rate of change in error $e(t)$, respectively [48].

A drawback with feedback control is that it relies on sensor-based measurement of output $y(t)$ to detect the onset of process drifts. Consequently, closed-loop control is inherently reactive in nature, and there is a lag before the process is returned to its nominal state [48]. In Table 1, we have summarized representative implementations of feedback control in LPBF reported in the literature stratified by the sensing technology, control strategy, and outcome.

Three challenges exist for applying closed-loop control strategies in LPBF. First, the delay in the feedback loop limits the scope of corrective action when there are sudden, large variations in the thermal history, such as in complex parts [48]. Second, sensors in LPBF can only acquire data from the top surface of the part, the thermal history of the bulk volume progressively covered by powder cannot be observed directly. Third, feedback control is practically difficult to implement in commercial LPBF systems given the lack of access to the machine controller. Therefore, commercial LPBF systems with an integrated feedback control mechanism are in their infancy [54–56]. For example, EOS recently introduced a closed-loop control system that dynamically adjusts the laser power to mitigate heat buildup, thus reducing the need for of support structures [56].

2.2 Open-Loop Feedforward Process Control (This Work). In purely feedforward control, sensor data measuring the output variable $y(t)$ are not used as an input to correct the process [47]. Instead, the process is adjusted based on a physics-based, empirical, or AI-based model that predicts the process output $\hat{y}(t)$ as a function of process input variables [47]. The control action is triggered by an anticipated disturbance in the process state. The disturbance may be measured by sensors on the input side of the process. Thus, the process adjustment occurs independent of output measurements $y(t)$. The controller adjusts the input parameters to minimize an anticipated drift from the setpoint $r(t)$; i.e., minimize the estimated error signal $\hat{e}(t) = r(t) - \hat{y}(t)$ [47]. The model guides the appropriate control action $u(t)$ to minimize $\hat{e}(t)$. Feedforward control is thus proactive and mitigates the lag inherent in feedback control. However, stochastic process drifts that affect the actual output $y(t)$ are not compensated in feedforward control.

In the LPBF context, process adjustments in feedforward control are made before printing based on predictions from an empirical or computational model, or combination of both [34,35]. The current work uses a physics-based computational thermal model to guide parameter adjustment. Select implementations of feedforward control in the LPBF literature are summarized in Table 2. These existing approaches predominantly focus on meltpool or hatch-level control of the thermal history [34,58,60]. While effective for relatively simple part geometries, such hatch- and meltpool-level prediction approaches would be intractable to implement in large, practical geometries. By contrast, this work applies a part-scale model predictive feedforward control approach, which as explained in the context of Fig. 3, is an iterative optimization method. The controller is based on a graph theoretic computational thermal model, which converges an order of magnitude faster than FE models on a desktop computer [36]. In closing this section, we note that practical industrial control systems use a hybrid feedback-feedforward control strategy. However, feedback control is challenging to implement in commercial LPBF machines due to original equipment manufacturer (OEM) restrictions.

3 Methodology

3.1 Experiment Setup. Stainless steel 316L (SS316L) parts were manufactured on an EOS M290 LPBF system. A schematic of the setup is shown in Fig. 5, and the nominal experimental conditions are reported in Table 3. The nominal processing conditions are chosen based on extensive process optimization studies with SS 316L conducted on the same machine, and reported in our previous work [63]. We note that none of the parts in this work showed evidence of a lack of fusion or keyhole porosity when examined with SEM, optical microscopy, and X-ray computed tomography (CT).

The system is instrumented with a long-wave infrared (LWIR) thermal camera. As shown in Fig. 5(*a*), the thermal camera is installed outside the build chamber approximately at an angle of 70 deg to the horizontal and at a distance of ~430 mm from the powder bed surface. The thermal camera is used to capture the top surface temperature of the build plate layer by layer at a rate of 30 frames per second. The thermal camera is calibrated to the real temperature scale through an industry-standard procedure [64]. The temperature data acquired by the thermal camera are used for validating the prediction accuracy of the graph theory thermal model.

3.2 Part Geometries and Build Plan. The build plate and part geometries manufactured in this work are shown in Fig. 6. Two

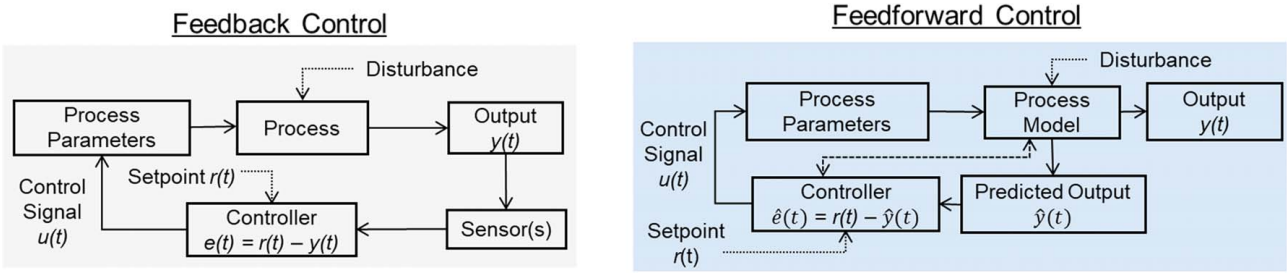

Fig. 4 Comparison of closed-loop feedback control and open-loop feedforward control strategies. This work implements feedforward control.

Downloaded from http://asmedigitalcollection.asme.org/manufacturingscience/article-pdf/147/8/081005/7500901/manu-25-1025.pdf by Virginia Polytechnic Institute and State University user on 27 June 2025

Table 1 Examples of feedback control approaches implemented in LPBF in the literature

Ref	Feedback sensors	Control strategy	Outcome
Wang et al. [49]	Coaxial photodiodes	Laser power is modulated via a PID controller to maintain the measured thermal emissions of the meltpool at a desired setpoint.	Approach was demonstrated on single-layered Inconel 625 parts. Feedback control mitigated surface defects, such as overmelting, swelling, and balling.
Renken et al. [50]	Coaxial pyrometer	Laser power is modulated via a proportional controller to maintain a desired meltpool emission as measured by a pyrometer.	Approach significantly reduced heat accumulation in a bridge-shaped part (steel) and significantly reduced layer temperature variation.
Vasileska et al. [51]	Coaxial imaging of the meltpool using an optical camera.	Laser power is modulated through duty cycle alteration to maintain a consistent meltpool shape and size in a feedback control arrangement.	Approach improved feature resolution of bridge-shaped parts (316L stainless steel).
Kavas et al. [52]	Off-axis infrared thermal camera to acquire the interpass surface temperature.	The interlayer temperature is controlled layer by layer by changing the laser power with a greedy optimization algorithm.	Reduced overheating and improved tensile strength in samples (316 stainless steel).
Adnan et al. [53]	Coaxial and off-axis optical camera	The meltpool emission was controlled by modulating the laser power and scan speed. Machine learning was used to determine the optimal processing parameters.	Improved tensile strength of subsequent layers in cuboid-shaped parts.

Table 2 Select examples of feedforward control implemented in LPBF in the literature

Ref.	Model type	Control approach	Outcome
Yueng et al. [57]	Empirical model-based approach	A geometric correction factor reduces the laser power when printing overhang regions.	Heat retention in the overhang was mitigated, which improved surface roughness in Inconel 625.
Druzgalski et al. [34]	FE-based hatch-level simulation	A library of computation modeling approaches predicts track quality. Laser power and other parameters are changed on a track-level heuristically.	Feedforward control was demonstrated on a complex stainless steel 316L part and showed improved surface finish and geometric integrity.
He et al. [58,59]	Semianalytical model-based hatch-level simulation	Various hatch-level scan strategies are simulated. The scan strategy with the most uniform thermal distribution is selected	The model-selected scan strategy reduces thermal-induced residual stresses and distortion in stainless steel 316L plate-like samples.
Wang et al. [60]	FE-based track-level model	An analytic, track-level model predicts the change in thermal history of an LPBF geometry with two and five layers, respectively.	Controlling the laser power on a track level enabled a reduction of keyhole porosity formation in Inconel 625 samples.
Ogoke et al. [61]	Empirical reinforcement machine learning to predict meltpool distribution	Reinforcement learning algorithm alters the process parameter conditions to maximize the time spent in an a priori identified optimal meltpool condition.	Controlling the process parameters reduced local overheating in simulation and stabilized meltpool depth. This study did not include experimental results.
Kusano and Watanabe [62]	FE-based part-level model	Model-based control of thermal history by altering time between layers	Controlling the time between layers reduced part temperature and showed ability to alter microstructure formation in IN 738LC

identical build plates were printed. A total of 16 parts were manufactured on each build plate, consisting of four unique geometries, these are labeled as cone (C), overhang (O), spring (S), and bell crank (B). All parts were 21 mm tall (525 layers). On the first build plate, shown in Fig. 6, each of the four parts was manufactured under four different thermal history control scenarios, labeled as $\mathbf{U}$, $\mathbf{K}T_e$, $\mathbf{\Delta}T_e$, and $\mathbf{K}t_r$. The fifth control strategy enforces a constant time between layers, labeled as $\mathbf{K}\tau$, and it is implemented on a second build plate identical to the one shown in Fig. 6. These thermal control strategies are described in detail in Sec. 4.4. In Fig. 6, a nomenclature is used to reference a specific part shape and its corresponding control strategy; e.g., $C(\mathbf{K}T_e)$ is a cone-shaped part manufactured with the $\mathbf{K}T_e$ thermal control strategy. The first build plate required 5 h to complete, and the build plate with a constant time between layers required 8 h.

A total of 20 parts were analyzed in this work (4 part geometries $\times$ 5 thermal history strategies). Representative as-received infrared thermal images for the first build plate are shown in Fig. 7. Note the prominent differences in surface temperature at layer 500 for the cone-shaped part processed with various thermal history

Downloaded from http://asmedigitalcollection.asme.org/manufacturingscience/article-pdf/147/8/081005/7500901/manu-25-1025.pdf by Virginia Polytechnic Institute and State University user on 27 June 2025

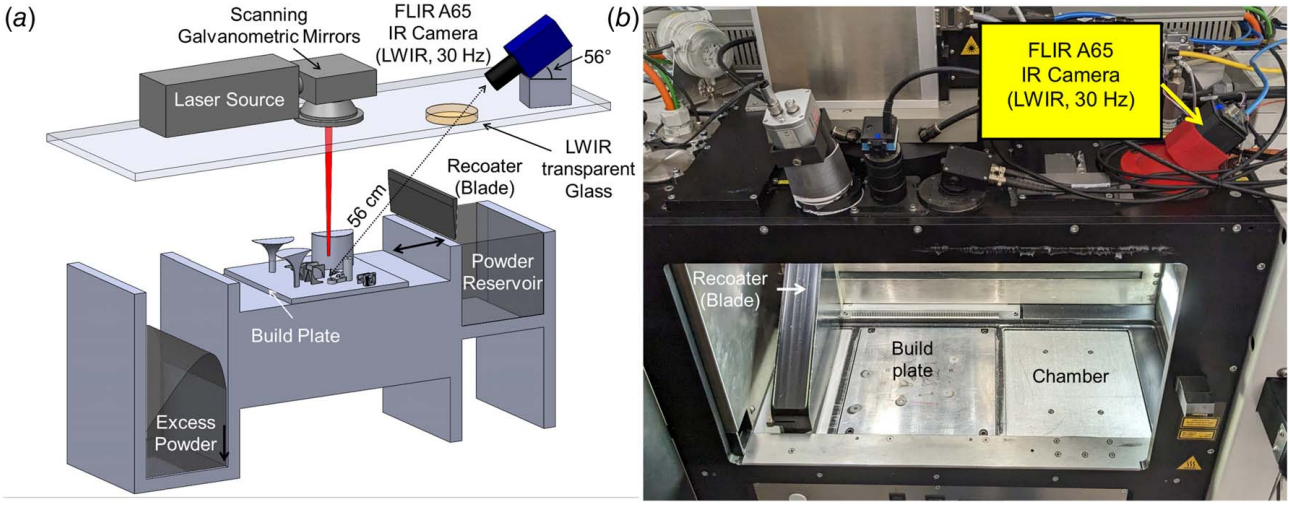

Fig. 5 (*a*) Schematic and (*b*) picture of the experimental LPBF setup with long-wave infrared thermal camera installed outside the build chamber

Table 3 Processing conditions, materials properties, and sensor settings used in this work

	Values
Process parameter (units)	
Nominal laser power, P (W)	230
Scanning velocity, V (mm/s)	928
Hatch spacing, H (mm)	0.09
Layer thickness, L (mm)	0.04
Nominal, volumetric global energy density, E_v (J/mm^3)	69
Build atmosphere	Argon
Build plate preheat temperature (°C)	70
Recoater cycle time (s)	10
Recoater blade type	Metal
Powder material properties	
Material type	Stainless Steel 316L
Material manufacturer	Oerlikon
Powder size range (μm)	15–45 (D10–D90)
IR thermal camera specifications	
Brand and model	Micro Epsilon 640
Resolution (pixels) (pixel/mm^2)	640 × 840, 13
Frame rate (Hz)	30
Spectral range (μm)	7.5–13
Temperature range (°C)	0–250
Camera on trigger event	Continuous

Note: The processing conditions are based on the prior work with SS 316L [63].

control strategies. The salient aspects of the four exemplar shapes are discussed herewith.

*3.2.1 Cone (*C*).* The cone (*C*) geometry has two 45 deg overhangs. The first overhang spans 12.5 mm (313 layers), the second spans the subsequent 8.5 mm (212 layers). As observed in our previous works, the latter layers of the cone tend to retain heat due to its progressively increasing surface area, resulting in grain coarsening [18].

*3.2.2 Overhang (*O*).* The overhang (*O*) geometry was studied in our recent work [30]. As first depicted in Fig. 2, the overhang region tends to retain heat, which results in grain coarsening and degraded surface roughness on the underside due to the adhering of partially melted powder, termed dross formation [65,66].

*3.2.3 Spring (*S*).* The spring (*S*) geometry has five overhang angles, ranging from 30 deg at the top to 50 deg at the bottom in 5 deg increments. The overhang regions of the part are susceptible to overheating, resulting in degradation of surface finish and geometric integrity due to dross formation and thermal-induced distortion, respectively.

*3.2.4 Bell Crank (*B*).* The bell crank (*B*) is a commonly used linkage mechanism in aerospace and automotive applications. The bell crank consists of a base and a cylindrical hollow shaft. The cavity contains an internal overhang region, which begins at 18.09 mm (452 layers) and is completed at 19.47 mm (487 layers). The surface of the internal overhang region is prone to dross formation on account of heat accumulation. This internal overhang is inaccessible for postprocess subtractive machining.

3.3 Postprocess Characterization. The complex geometries manufactured in this work are not amenable for mechanical testing. Therefore, in lieu of mechanical testing we have characterized the geometry, surface integrity, and microstructure in the form of primary dendritic arm spacing.

3.3.1 Geometry and Surface Integrity. The surface roughness of the underside of the overhang geometry was ascertained using a laser confocal microscope (Keyence VK-X 3000). The instrument was also used to measure geometric integrity of the spring-shaped part. As demarcated in Fig. 8(*a*), the distance of the five corners of the spring part to its base was measured, and geometric deviation was quantified by comparing the measured distances to the computer-aided design (CAD) design. X-ray computed tomography (North Star Imaging X3000) was used to examine the geometric integrity of the internal surface of the bell crank at a resolution of 16 μm.

3.3.2 Microstructure—Primary Dendritic Arm Spacing (λ_1). The spring (*S*), overhang (*O*), and cone (*C*) geometries were cross sectioned vertically along the build direction for metallurgical analysis using electrodischarge machining. The samples were progressively ground with 300–1200 grit size silicon carbide-fixed abrasive pad and subsequently polished to mirror finish using 6 μm and 1 μm diamond suspension and 0.05 μm colloidal silica abrasive slurry. The polished parts were etched with aqua regia (3:1 = HCl:HNO_3) for 4–5 min. The microstructure of stainless steel 316L LPBF parts is typically columnar dendritic in nature; a columnar dendritic microstructure was observed in all parts of this work [67]. The grain size of columnar dendrites was quantified

Downloaded from http://asmedigitalcollection.asme.org/manufacturingscience/article-pdf/147/8/081005/7500901/manu-25-1025.pdf by Virginia Polytechnic Institute and State University user on 27 June 2025

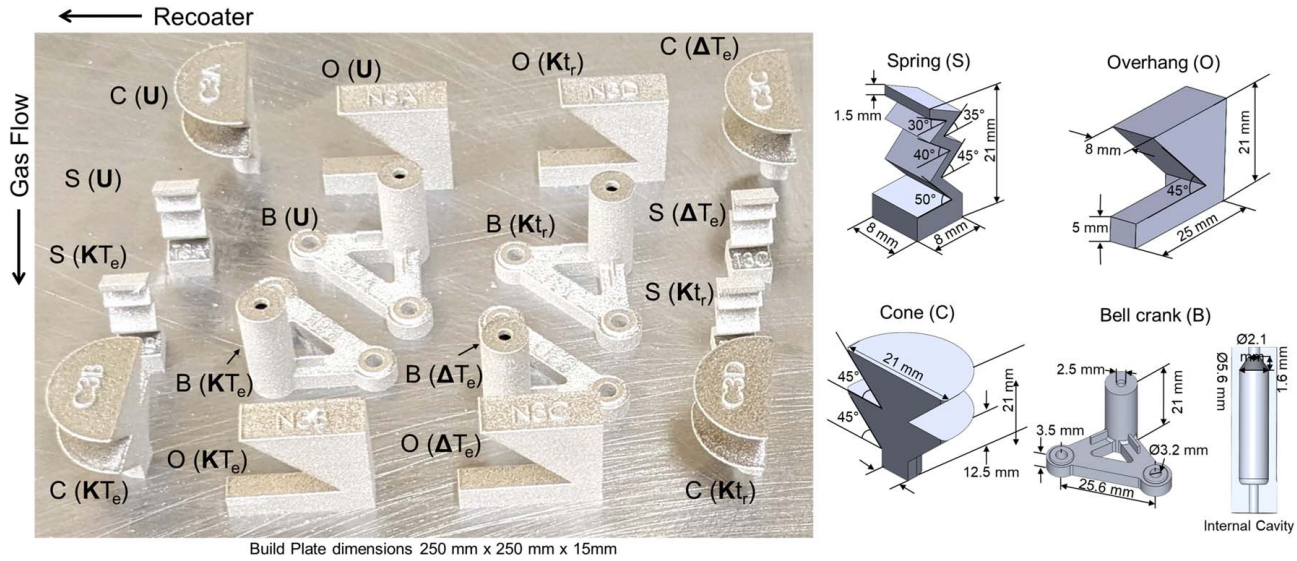

Fig. 6 Picture of the build plate. Four part shapes are studied in this work, cone (*c*), spring (*S*), and overhang (*O*), and bellcrank (*B*). Each part is built under different thermal control strategies, labeled as U, KT$_e$, ΔT_e, Kt$_c$, and, Kτ, discussed in Sec. 4.4.

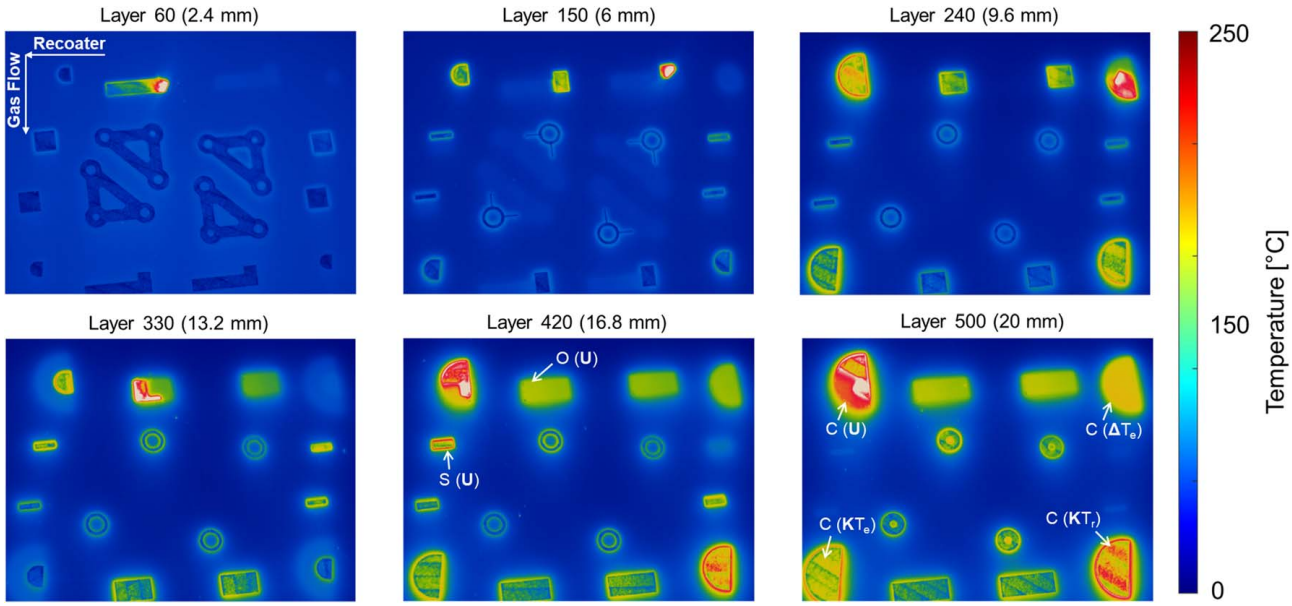

Fig. 7 Uncalibrated surface temperature images obtained from the IR camera during the build. These images are taken as the laser is melting a layer. Note the difference in the thermal history between the four cone-shaped parts on account of various feed-forward control strategies.

in terms of the PDAS (λ_1). The PDAS affects mechanical properties, e.g., a smaller grain size is correlated with improved tensile strength and creep resistance [68,69].

To measure PDAS, the samples were examined with SEM (Jeol IT-500HR). The PDAS was measured for the spring (*S*), overhang (*O*), and cone (*c*) geometries at the locations demarcated in Figs. 8(*a*)–8(*c*), respectively; 11 locations were analyzed for each of the five spring-shaped parts, 10 locations for each overhang, and 12 locations for each cone. At each location, two SEM images were acquired, and PDAS measurements were acquired for two different regions within each image. Thus, 44 PDAS measurements are acquired for each spring part; 40 for overhang; and 48 for the cone. The PDAS measurements from SEM images were obtained using the industry-standard bounding box procedure detailed in our previous works [30]. For later analysis, the overhang (*O*) geometry is divided into four regions, which are 5.25 mm apart, and the cone (*c*) is divided into six regions, 3.25 mm apart. Further, no porosity was observed in any of the parts. We note that none of the SEM images for any of the parts showed the presence of either keyhole or lack-of-fusion porosity. Further, SS 316L is not a heat-treatable alloy and does not show any other material phases besides γ austenite, and hence, X-ray diffraction to ascertain phases would not be warranted.

4 Process Control

4.1 Graph Theory Thermal Modeling. The FE method is typically used to predict thermal history in LPBF [38–40,70]. However, the computationally intensive nature of FE analysis

Downloaded from http://asmedigitalcollection.asme.org/manufacturingscience/article-pdf/147/8/081005/7500901/manu-25-1025.pdf by Virginia Polytechnic Institute and State University user on 27 June 2025

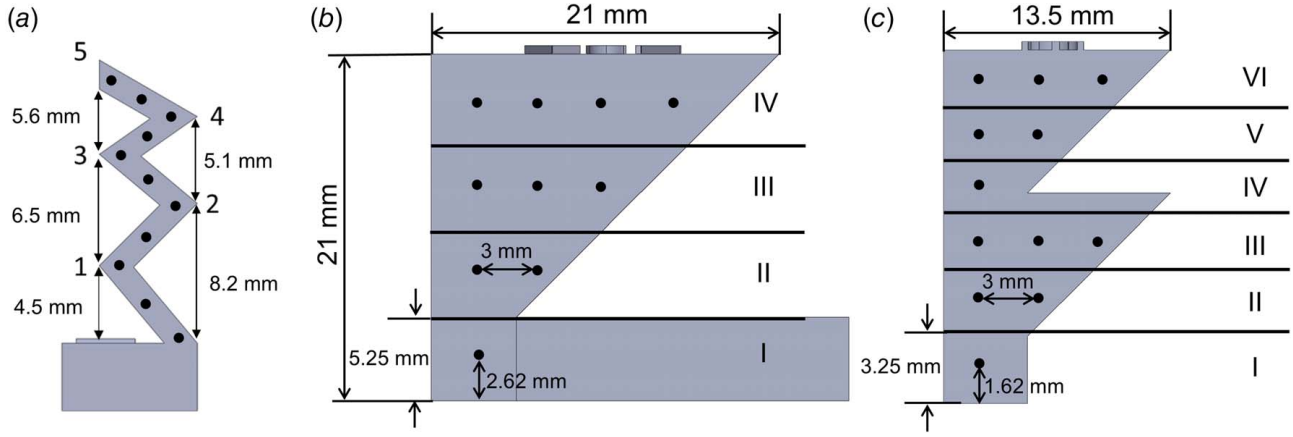

Fig. 8 (*a*) Measurement locations for quantifying distortion in the spring geometry labeled 1–5; the dots represent measurement locations for the PDAS (λ_1) with SEM. (*b*) and (c) Locations on the overhang and cone samples where SEM images were acquired to measure λ_1.

renders it unsuitable for the iterative nature of the model predictive thermal history control approach implemented in this work [38–40,70]. Consequently, a mesh-free, rapid graph theory approach is used for predicting the thermal history [33,71]. The approach has been comprehensively detailed in our prior publications including verification with FE and Green's function analytical solutions, as well as experimentally validated with in situ infrared thermal imaging data [33,36,64,72]. Herewith, we provide a brief summary of the approach.

The graph theory approach seeks to predict the temperature T at every sampled point (x,y,z) in the part at time (t). This relationship is described by the heat diffusion equation, Eq. (1).

$$\rho c_p \frac{\partial T(x,y,z,t)}{\partial t} - k\overbrace{\left(\frac{\partial^2}{\partial x^2}+\frac{\partial^2}{\partial y^2}+\frac{\partial^2}{\partial z^2}\right)}^{Laplacian\ operator} \mathrm{T}(x,y,z,t) = \mathrm{Q} \qquad (1)$$

In Eq. (1), ρ is the material density (kg/m^3), c_p is the specific heat (J/kg/K), k is the conductivity (J/s/m/K), and Q is the rate of heat supplied per unit volume of material melted (J/s/m^3), called volumetric heat flux. Material properties are assumed to be fixed and are evaluated at 250 °C. The term $Q = A_e \frac{P}{V \cdot H \cdot L \cdot t_l}$ (W/mm^3) is the heat input from laser heating and encompasses the following parameters: laser power (P (W)), laser velocity (V (m/s)), hatch spacing (H (m)), layer height (L (m)), laser absorptivity (A_e), and t_l (s) is the time the laser is active. To aid rapid computation, the graph theory modeling approach replaces the continuous Laplacian operator $\left(\frac{\partial^2}{\partial x^2}+\frac{\partial^2}{\partial y^2}+\frac{\partial^2}{\partial z^2}\right)$ in Eq. (1), with its discrete equivalent Laplacian matrix (L). The graph theory implementation in the context of LPBF processing of the cone-shaped part is shown in Fig. 9.

Referring to Fig. 9, the graph theory thermal model represents the spatial domain of the continuous Laplacian through discrete points, termed nodes. These points are related to each other through edges. The resulting network graph captures the effect of geometry on heat transfer between nodes. The graph theory approach models the heat flow through the nodes and edges after the top surface is heated by the laser through Eq. (2). This process is repeated, layer by layer, resulting in the complete thermal history for the geometry [33,41,71].

The graph theory approach essentially solves a discrete spatial version of the heat diffusion equation Eq. (1). The thermal history $T(x,y,z,t)$ is obtained as a function of the eigenvalues (Λ) and eigenvectors (ϕ) of the Laplacian matrix (L) as follows [33]:

$$T(x,y,z,t) = \overbrace{\phi e^{-\frac{k}{\rho c_p}\Lambda tg}\phi'}^{Part\ shape\ and\ time} \overbrace{\left(\frac{A_e S_l}{\rho v c_p}\frac{P}{V}+\hat{T}_{\mathrm{prev}}\right)}^{Processing\ conditions} \qquad (2)$$

In Eq. (2), the thermal history of the part $T(x,y,z,t)$ is written as independent functions of the part shape and the LPBF processing conditions. The solution is semi-analytic in nature, i.e., discrete in space and continuous in time. In Eq. (2), the process parameters considered for laser heating include laser power, P (W), laser velocity, V (mm/s), and volume of material melted in a layer, v (mm^3) (a product of scanned area and layer height). S_l is the estimated length of the scan path, namely, a function of the part surface area (mm^2) and hatch spacing (mm). The laser absorptivity, $A_e = 0.6$, was fixed based on experiments by Ye et al. [73]. The time for cooling (t) is determined by the time between layers or ILT (τ), which is detailed in Sec 4.4.4. The unitless gain factor $g = 0.6$ is used to scale the cooling behavior of the graph theory model; g is maintained identical to our previous works [30]. The importance and nature of g is described by Cole et al. [33].

There are three computational advantages to the graph theory approach that enables its use for model predictive control.

(1) The graph theory approach eschews the need for cumbersome meshing steps required in FE analysis.
(2) In Eq. (2), temperatures T at any location (x,y,z) and time instant t can be obtained, eliminating the need for the simulation to step through time, significantly reducing the computational load.
(3) In solving the heat equation in Eq. (2), the effect of part shape and cooling time (t) are entirely decoupled from the processing conditions, such as laser power (P) and scan velocity (V). As a result, the spatial component, i.e., the eigenvalues (Λ) and eigenvectors (ϕ) of the Laplacian matrix (L), for each part layer can be precalculated and stored in computer memory. Consequently, the effect of different process parameters can be iterated without the need for repeated re-meshing, required in FE techniques [41].

4.2 Thermal Model Calibration and Validation. It is necessary to calibrate the boundary conditions of the graph theory model, specifically in terms of the following three heat transfer coefficients: (i) heat loss from the part to the build plate (h_s); (ii) heat loss by radiation and forced convection to the gas (h_g); and (iii) heat loss to the surrounding powder (h_p) [39]. Heat losses are considered in the graph theory thermal simulation by adjusting the Laplacian matrix with type 3 (convection) boundary conditions [33]. These

Downloaded from http://asmedigitalcollection.asme.org/manufacturingscience/article-pdf/147/8/081005/7500901/manu-25-1025.pdf by Virginia Polytechnic Institute and State University user on 27 June 2025

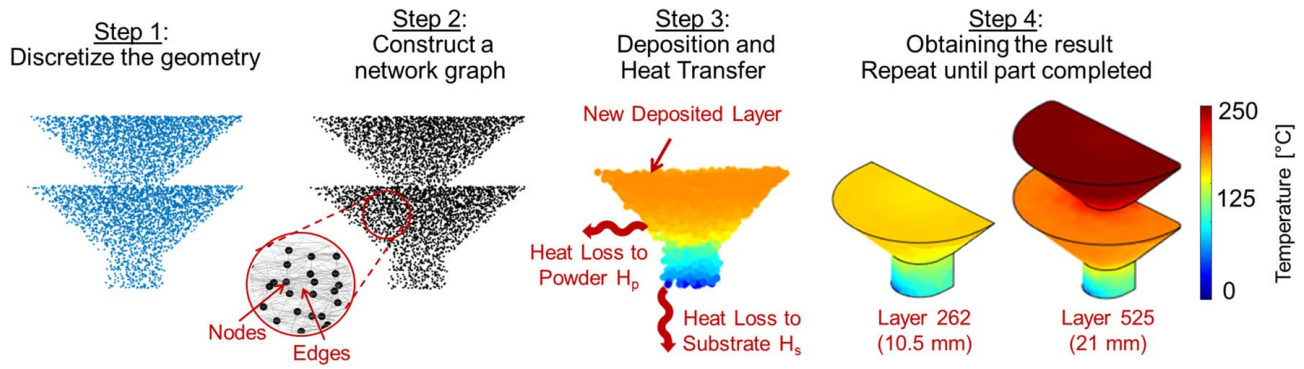

Fig. 9 Application of graph theory thermal modeling in the context of the cone part

boundary conditions are calibrated by comparing the model-predicted top surface temperature to experimentally obtained measurements from the IR thermal camera. These heat transfer coefficients were calibrated a priori on the same machine and material with different parts and used as is for this work. The data and geometries used for model calibration are discussed in our prior publication [45].

The IR camera was calibrated using reference thermocouple measurements as described in our previous works [18,41,45]. The IR image after calibration is shown in Fig. 10(*a*). The IR temperature measurements acquired over six layers for a region of interest for one of the cone-shaped parts—$c(\mathbf{K}t_r)$—is shown in Fig. 10(*b*). The sharp peaks are a result of the laser passing over the region of interest. An important thermal history characteristic called the average end-of-cycle temperature (T_e) is extracted from the time series shown in Fig. 10(*b*). This metric T_e is used for validating the model predictions; it is analogous to the interpass temperature from welding [74]. In one of our recent works, T_e was correlated to microstructure evolution in LPBF-processed 316L parts [63].

To estimate T_e, first, the top surface temperature is obtained at each location on a part after a layer of powder has been deposited but is yet to be melted. The end-of-cycle temperature at each region of interest is denoted in Fig. 10(*b*). The end-of-cycle temperature consolidated as an image for an exemplar layer is shown in Fig. 10(*c*). The layer-averaged end-of-cycle surface temperature (T_e) trend for a specific part $c(\mathbf{K}t_r)$ is shown in Fig. 10(*d*).

In Fig. 11, T_e measured from the IR camera images is compared to the model-predicted ($\hat{T}_e$) for each of the four geometries, produced under the nominal or uncontrolled (**U**) processing conditions. The symmetric mean absolute percentage error (SMAPE) comparing model predictions to IR observations is within 5% for all geometries. The root-mean-squared error (RMSE) ranged from 4 °C to 15 °C. The simulation time for a single iteration ranges from 1 min for the overhang to 7 min for the spring. The parameters used for the simulations are reported in Table 4.

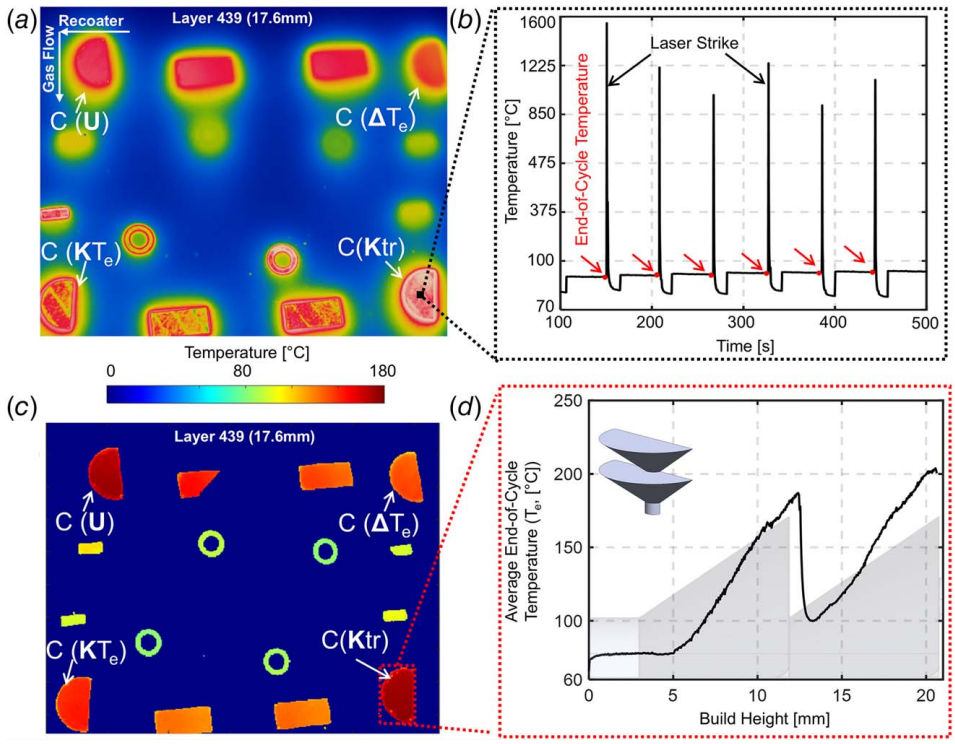

Fig. 10 The process to extract the average end-of-cycle temperature (T_e) from the infrared camera. (*a*) Calibrated top surface temperatures are extracted from the IR camera. (*b*) Surface temperature measurements at a region of interest. (c) The end-of-cycle temperature is obtained for all pixels in the image, resulting in a composite image for a complete layer. (*d*) T_e is obtained by averaging the surface temperature for the entire layer of a part.

Downloaded from http://asmedigitalcollection.asme.org/manufacturingscience/article-pdf/147/8/081005/7500901/manu-25-1025.pdf by Virginia Polytechnic Institute and State University user on 27 June 2025

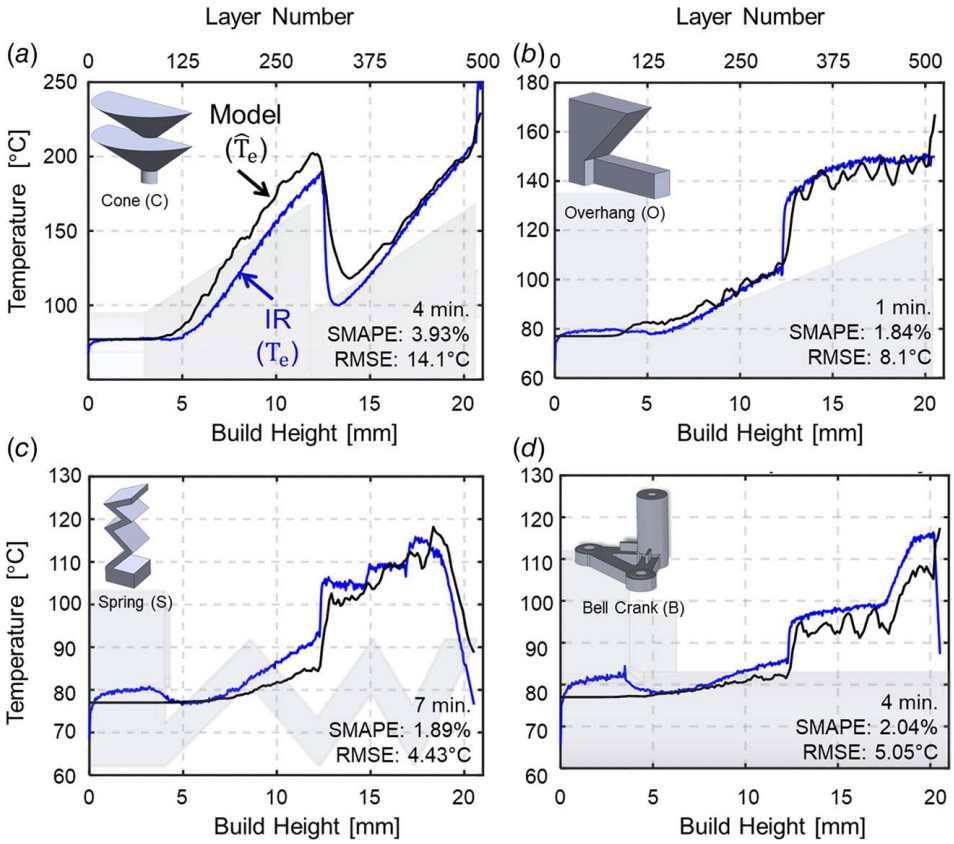

Fig. 11 Comparison of the end-of-cycle surface temperature ($\hat{T}_e$) predicted by the model and measured from IR readings (T_e) for (*a*) cone, (*b*) overhang, (c) spring, and (*d*) bell crank geometries

Table 4 Simulation parameters obtained after model calibration

Simulation parameters	Values
Heat loss coefficient part to powder, h_p (W/m^2 °C)	8
Heat loss coefficient part to substrate, h_s (W/m^2 °C)	20,000
Heat loss coefficient to gas flow, h_g (W/m^2 °C)	10
Thermal conductivity (k) (W/m °C)	17
Density (ρ) (kg/m^3)	8193
Specific heat (c_p) (J/kg/°C)	540
Melting point (°C)	1609
Ambient chamber temperature (°C)	77
Node density (nodes mm^3)	2.25
Superlayer thickness (mm)	0.12 (3 actual layers)
Gain factor (g) (unitless)	0.6
Computational hardware	AMD Ryzen 3970X CPU, @3.70 GHz

4.3 Model Predictive Control. The key idea of model predictive control is to iteratively optimize laser power (P) over a fixed time horizon (number of layers). The model is subject to constraints on the adjustable levels of P [31,32]. The approach, explained with the aid of a schematic diagram in Fig. 12, consists of four steps. These steps are demarcated as Predict, Identify, Parse, and Select; they are elucidated herewith in the context of the cone-shaped part.

4.3.1 Step 1: Predict. Given a part shape, orientation on the build plate, support structures, material properties, time between layers, and nominal processing conditions, the graph theory approach is used to predict the thermal history trends. In Fig. 12, the end-of-cycle temperature for nominal or uncontrolled condition is plotted as a red dotted line and labeled as $\hat{T}_{\text{original}}$. For illustration purposes, in Fig. 12, $\hat{T}_{\text{original}}$ indicates heat accumulation in the latter layers.

4.3.2 Step 2: Identify. Next, the ideal thermal history ($\hat{T}_{\text{ideal}}$) or target thermal history is identified. In Fig. 12, $\hat{T}_{\text{ideal}}$ is represented as a solid black line. $\hat{T}_{\text{ideal}}$ is selected in a manner such that it mitigates the deleterious temperature buildup identified in $\hat{T}_{\text{original}}$ from step 1. In this work, four strategies are presented in Sec. 4.4 to identify $\hat{T}_{\text{ideal}}$.

4.3.3 Step 3: Parse. Step 3 alters the original thermal history ($\hat{T}_{\text{original}}$) layer by layer as a function of laser power levels $P(\theta_i)$, so as to match the ideal thermal history ($\hat{T}_{\text{ideal}}$). The adjusted thermal history ($\hat{T}_P$) is considered for a fixed (k) number of future layers, called the prediction horizon or lookahead. A prediction horizon is necessary to ensure that the corrected thermal history $\hat{T}_P$ does not overshoot $\hat{T}_{\text{ideal}}$. For layer N of the part, the thermal history $\hat{T}_{P(\theta_i)}$ is predicted as a function of h candidate laser power settings $P(\theta_i)$ for k future layers, $i = \{1 \ldots h\}$, herein $h = 5$ and $k = 5$. Thus, in step 3, the thermal history is predicted from the graph theory thermal model for layers N to $N+k$ as a function of laser power $P(\theta_i)$, i.e., $\hat{T}_{P(\theta_i)}(N+0)$, $\hat{T}_{P(\theta_i)}(N+1) \ldots \hat{T}_{P(\theta_i)}(N+k)$.

In effect, a grid search is conducted as a function of h laser power levels, as depicted by the dashed blue lines in Fig. 12. The five discrete laser power (P) settings tested were as follows: $P(\theta_1) = 180$ W, $P(\theta_2) = 198$ W, $P(\theta_3) = 214$ W, $P(\theta_4) = 230$ W, and $P(\theta_5) = 240$ W, noting that $(\theta_4) = 230$ W is the nominal laser power. The laser power is constrained between $182 \text{ W} \le P \le 245$ W to avoid lack-of-fusion porosity at the lower bound and keyhole porosity at the higher bound [37]. These constraints were obtained from screening experiments conducted a priori [63]. We note that none

Downloaded from http://asmedigitalcollection.asme.org/manufacturingscience/article-pdf/147/8/081005/7500901/manu-25-1025.pdf by Virginia Polytechnic Institute and State University user on 27 June 2025

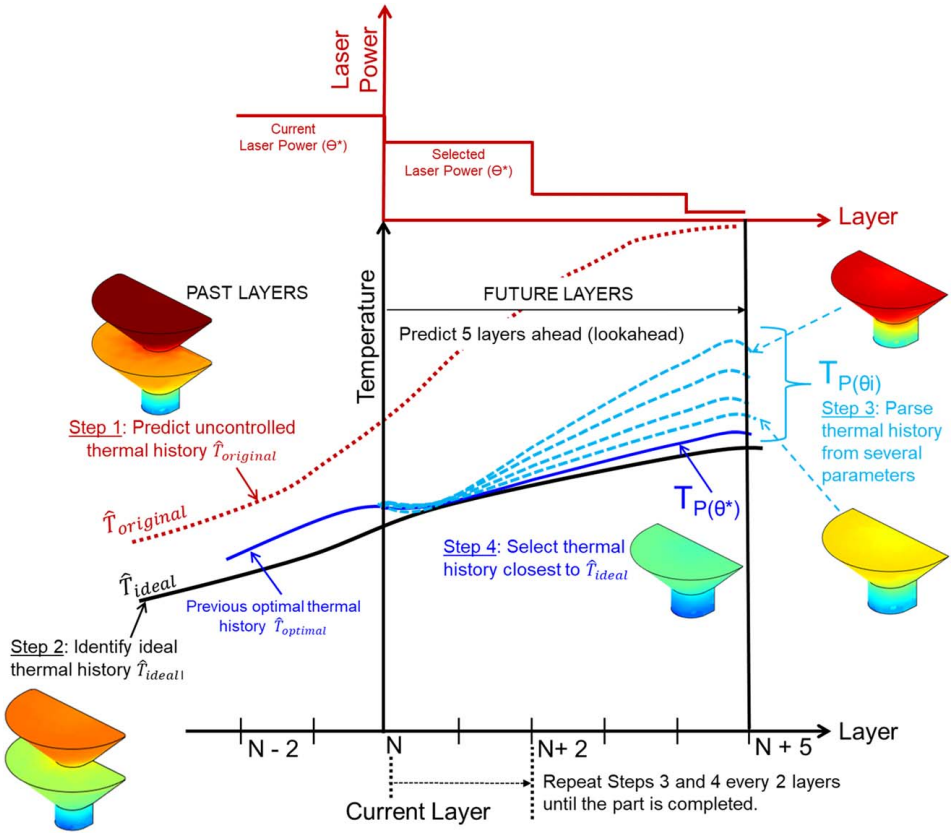

Fig. 12 Summary of the model predictive control approach in the context of LPBF. The process is divided into four steps: (1) predict, (2) identify, (3) parse, and (4) select.

of the parts in this work showed evidence of lack of fusion or keyhole porosity when examined with SEM, optical microscopy, and X-ray CT.

4.3.4 Step 4: Select. After the thermal history $\hat{T}_{P(\theta_i)}$, $i = \{1 \ldots 5\}$ for each of the five laser power levels are simulated, we select the optimal laser power (θ^*), which results in the minimum mean absolute deviation (MAD) between $\hat{T}_{\text{ideal}}$ and $\hat{T}_{P(\theta_i)}$ over the prediction horizon $k = 5$. Mathematically, the control objective function is expressed as follows:

$$P(\theta^*) = \underset{\substack{\theta \\ \theta = \{\theta_1 \ldots \theta_5\}}}{\arg\min} \sum_{k=1}^{k=5} \frac{|\hat{T}_{\text{ideal}}(N+k) - \hat{T}_{P(\theta)}(N+k)|}{k} \quad (3)$$

Thus, the optimal thermal history for layer N is $\hat{T}_{\text{optimal}}(N) = \hat{T}_{P(\theta^*)}$. It is represented as the solid dark blue line in Fig. 12.

Steps 3 and 4 are repeated for every two simulated layers, i.e., in Eq. (3), N is replaced by $N+2$ in the next step. In model predictive parlance, the foregoing simulation interval of two layers is termed the control horizon. Since each simulated layer represents three actual layers, each layer being 40 μm deep, the optimal laser power is determined every 240 μm of build height (control horizon). The model predictive control strategy autonomously determined the optimal laser power for the cone part in less than 4 h. The control approach is formally summarized as an optimization problem as follows:

Objective Function:

$$\hat{T}_{P(\theta^*)}(N) = \min \sum_{k=1}^{k=5} \frac{|\hat{T}_{\text{ideal}}(N+k) - \hat{T}_{P(\theta)}(N+k)|}{k}$$

where $\hat{T}_{\text{ideal}}$ is the ideal thermal history identified in step 1, $\hat{T}_{P(\theta)}$ is the predicted thermal history parsed in step 3, N is the current layer number, $N = 1 \ldots$total number of layers, and k is the prediction horizon ($k = 5$).

Decision Variable and Constraints:

Laser power, $P(\theta)$, $\theta \in \{182$ W, 198 W, 214 W, 230 W, 246 W$\}$

To aid practical implementation, two further simplifications are made to the completed power plan provided by the controller. Studies showed minimal differences in the thermal history for the as-predicted and simplified power plans.

(i) Since sudden changes in laser power can lead to cracking, a 10-point moving average (30 layers, 1.2 mm) is applied to the laser power plan generated by the controller.
(ii) Currently, the layerwise optimized laser power settings must be manually entered into the LPBF system before printing. To ease implementation, the laser power recommendations were further averaged for every 0.96 mm window of build height (24 layers).

4.4 Thermal History Control Strategies. Besides the nominal or uncontrolled (**U**) scenario, where the laser power is maintained fixed at $P = 230$ W for the entire part, four thermal history control strategies were examined in this work. In the model predictive control context, these strategies determine the desired thermal history trend $\hat{T}_{\text{ideal}}$ in step 2 (Fig. 12). Each of these four strategies is described herewith.

*4.4.1 Strategy 1—Maintain Constant End-of-Cycle Temperature (**K**T_e).* The constant end-of-cycle temperature scenario, represented as (**K**T_e), sets an upper bound on the end-of-cycle temperature (T_e) to a specific value. The laser power is reduced only when T_e increases above this threshold; T_e excursions below the target are ignored by the controller.

The implementation of the **K**T_e strategy is shown in Fig. 13(*a*) in the context of the cone geometry. The target end-of-cycle temperature ($\hat{T}_{\text{ideal}}$) for this strategy was set on a per-part basis. The $\hat{T}_{\text{ideal}}$

Downloaded from http://asmedigitalcollection.asme.org/manufacturingscience/article-pdf/147/8/081005/7500901/manu-25-1025.pdf by Virginia Polytechnic Institute and State University user on 27 June 2025

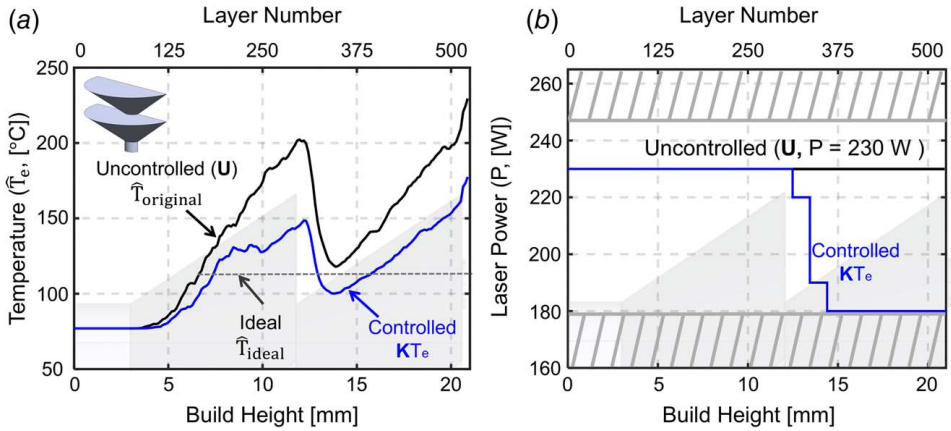

Fig. 13 Implementation of the constant end-of-cycle temperature strategy (KT_e) for the cone-shaped part. (*a*) KT_e significantly reduces the end-of-cycle temperature (T_e) compared to the uncontrolled (*U*) condition. (*b*) Power plan generated by the controller. Note the reduction in the laser power after 12.5 mm build height to avoid heat accumulation.

temperature is set as the average of the uncontrolled $\hat{T}_{original}$ over the entire part. For the cone-shaped part $\hat{T}_{ideal} = 110°C$. The $\mathbf{K}T_e$ strategy is compared to the uncontrolled thermal history (**U**, $\hat{T}_{original}$) in Fig. 13(*a*); the $\mathbf{K}T_e$ strategy significantly mitigates the peak end-of-cycle temperature. Shown in Fig. 13(*b*) are the layerwise laser power changes recommended by the model predictive control algorithm within bounds 182 W $\leq P \leq$ 246 W). The controller rapidly reduces the laser power at a build height of 12.5 mm (312 layers) to the lower limit of $P = 182$ W.

4.4.2 Strategy 2—Control (Minimize) End-of-Cycle Spatial Temperature Gradient ($\boldsymbol{\Delta}T_e$). The end-of-cycle temperature gradient control strategy, represented as $\boldsymbol{\Delta}T_e$, aims to minimize positive spatial gradients in the end-of-cycle temperature. The rationale is based on the observation that sharp increases in temperature between layers often result in flaws, such as cracking, thermal-induced distortion, and recoater crashes [75,76]. The spatial temperature gradient is estimated by averaging the slopes of the end-of-cycle temperature predictions ($\hat{T}_e$) from the present layer to five future layers. Only positive slopes exceeding 1 °C per layer are identified for mitigation by reducing the laser power. The ideal spatial temperature gradient ($\hat{T}_{ideal}$) is 0 °C per layer.

Shown in Fig. 14(*a*) is the effect of the $\boldsymbol{\Delta}T_e$ strategy on the end-of-cycle temperature ($\hat{T}_e$) in the context of the cone-shaped part. Compared in Fig. 14(*a*) are the $\hat{T}_e$ predictions for gradient control ($\boldsymbol{\Delta}T_e$) and uncontrolled (**U**) strategies. A significant decrease in peak end-of-cycle temperature is achieved as a result of $\boldsymbol{\Delta}T_e$. The layerwise changes in laser power implemented by the model predictive control strategy are depicted in Fig. 14(*b*). The $\boldsymbol{\Delta}T_e$ controller initiates a reduction in laser power at approximately 6 mm build height (150 layers), and in comparison, the previous $\mathbf{K}T_e$ strategy modified the laser power starting at 12.5 mm build height (320 layers).

4.4.3 Strategy 3—Maintain Constant Cooling Rate ($\boldsymbol{K}t_r$). In our previous work, the cooling rate (t_r) was correlated to grain size (PDAS, λ_1) of LPBF-processed Inconel 718 parts and Stainless Steel 316L [30,63]. A stable cooling rate was observed to mitigate microstructure heterogeneity. In this work, we control the cooling rate in terms of a thermal history metric called cooling time (t_c), namely, the inverse of the cooling rate (t_r).

The cooling time (t_c (s)) is obtained through the method illustrated in Fig. 15(*a*). The cooling curve predicted by the thermal simulation for one layer of the cone-shaped part is shown in this figure. The peak of the cooling curve is the temperature at the instant of the laser strike. The peak temperature rapidly reduces to the end-of-cycle temperature (T_e). The cooling time t_c is the duration for the temperature of the cooling curve to reach 700 °C, namely, approximately 0.5× liquidus of SS316L (1320 °C).

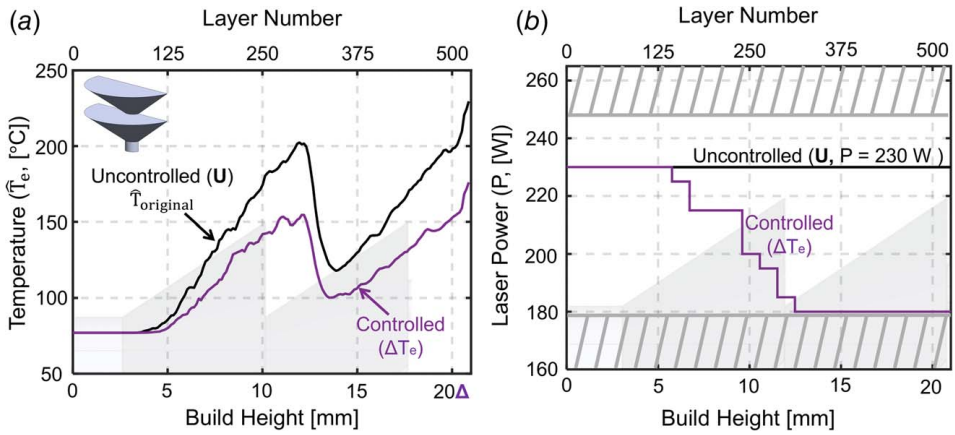

Fig. 14 Implementation of the end-of-cycle temperature gradient control strategy (ΔT_e) for the cone-shaped part. (*a*) ΔT_e significantly reduces the end-of-cycle temperature (T_e) compared to the uncontrolled (*U*) condition. (*b*) Power plan generated by the controller. Note the reduction in the laser power after 6 mm build height to avoid heat accumulation.

Downloaded from http://asmedigitalcollection.asme.org/manufacturingscience/article-pdf/147/8/081005/7500901/manu-25-1025.pdf by Virginia Polytechnic Institute and State University user on 27 June 2025

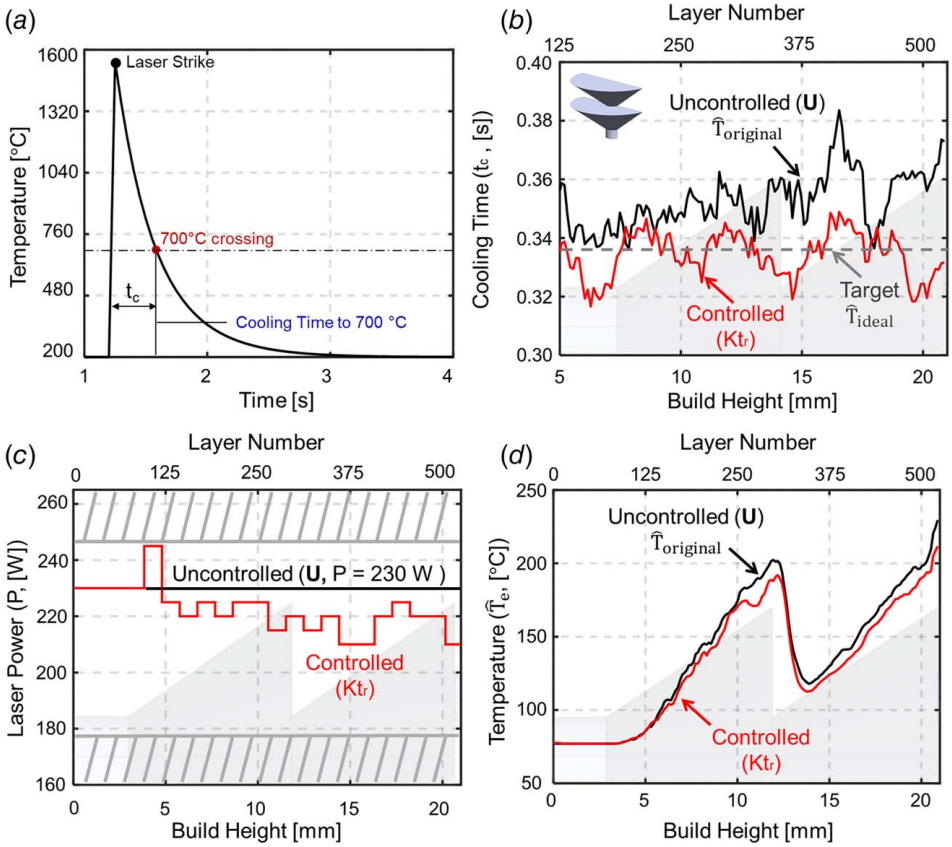

Fig. 15 (*a*) Obtaining the cooling time (t_c) from the cooling curve predicted by the thermal model. (*b*) Implementation of the constant cooling rate strategy (Kt_r) on the cooling time t_c for the cone-shaped part. ΔT_e maintains the average t_c at the target value of 0.34 s. (*c*) Power plan generated by the controller. Note the fluctuation in the laser power. (*d*) The end of cycle temperature (T_e) for Kt_r compared to the uncontrolled (*U*) condition. There is a minimal difference in T_e between Kt_r and U.

The constant cooling rate strategy, represented as $\mathbf{K}t_r$, aims to maintain t_c at a predetermined constant value. The target t_c was set as the weighted average of the minimum and maximum predicted cooling time for the uncontrolled scenario, with the minimum cooling time receiving a 75% weighting. Predicted cooling times for the first 5 mm were neglected, as the build plate acts is a heat sink that rapidly conducts heat in the base layers, thus biasing the trends in the bulk part.

The effect of the $\mathbf{K}t_r$ control strategy is shown in Fig. 15(*b*) for the cone-shaped part. The control target $t_c \approx 0.335$ s. Unlike previous cases, the $\mathbf{K}t_r$ controller activates when the predicted cooling time either exceeds or falls under the target. Reported in

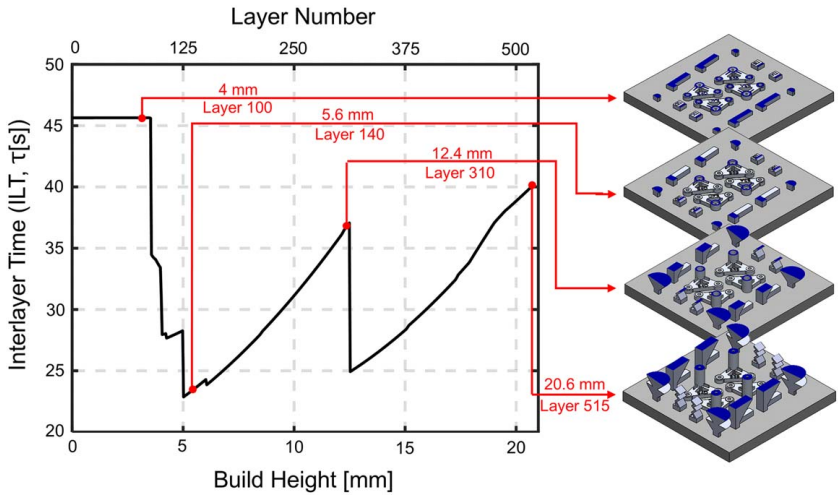

Fig. 16 The time between layers or interlayer time varies between 46 s and 22 s. The ILT is proportional to the surface area melted by the laser. The total build time was 5 h.

Downloaded from http://asmedigitalcollection.asme.org/manufacturingscience/article-pdf/147/8/081005/7500901/manu-25-1025.pdf by Virginia Polytechnic Institute and State University user on 27 June 2025

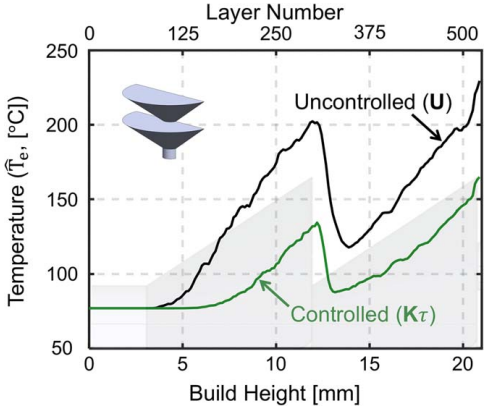

Fig. 17 Effect of maintaining a constant ILT of $\tau = 57$ s on the end-of-cycle temperature (T_e). Compared to the uncontrolled condition (U), the Kτ strategy significantly reduced heat buildup, albeit at the cost of build time, which increased from 5 h to over 8 h.

Fig. 15(*c*) are the layerwise laser power modulations implemented by the controller. The effect of implementing the $\mathbf{K}t_r$ strategy on the end-of-cycle temperature (T_e) is shown in Fig. 15(*d*); there is no significant difference in the end-of-cycle temperature T_e between $\mathbf{K}t_r$ and **U**. This is because the laser power adjustments in Fig. 15(*c*) does not drastically deviate from the nominal.

4.4.4 Strategy 4—Maintain Constant Interlayer Time (Kτ*).* ILT (τ (s)) is the duration between the start of melting of a certain location on a proceeding layer to start of scanning of the same location on a succeeding layer. The ILT is often referred to as TBLs or interpass time. The ILT encompasses the time required for the recoater to deposit a layer of powder, namely, 10 s. The ILT is not constant, but changes layer by layer in proportion to the surface area melted by the laser. The ILT is explicitly considered in the graph theory simulation in Eq. (2), where the time-step t aggregates to τ.

The ILT is an important aspect of the build condition and influences the thermal history [64]. A longer ILT allows the parts to cool for a longer duration. Conversely, low ILT increases the bulk part temperature. Hence, shorter ILT exacerbates heat retention and is liable to result in grain coarsening and recoater crashes [41]. Adding or removing parts from a build plate will change the ILT and consequently influence the microstructure [64]. Large variation in ILT have been linked to microstructure heterogeneity and cracking [67,77]. Therefore, it is often rationalized that maintaining a constant ILT throughout the build could mitigate thermal-induced errors. However, maintaining a constant ILT effects all the parts on the build plate and considerably increases the build time.

The ILT from the first build plate is shown in Fig. 16. These ILT data were estimated a priori based on the CAD design of the build plate, hatch spacing, and scan velocity; it was also verified postprocess with IR imaging data. At the start of the build, the ILT was approximately 45.6 s per layer. The ILT is reduced to 22 s at 5 mm of build height as the broad section of the parts is completed. The ILT gradually increases to 36 s, before dropping sharply to 25 s at 12.5 mm build height, at the completion of the first overhang of the cone-shaped geometry.

To maintain a constant ILT, a second build plate was created using identical parts to the build plate shown in Fig. 6, Sec. 3.1.

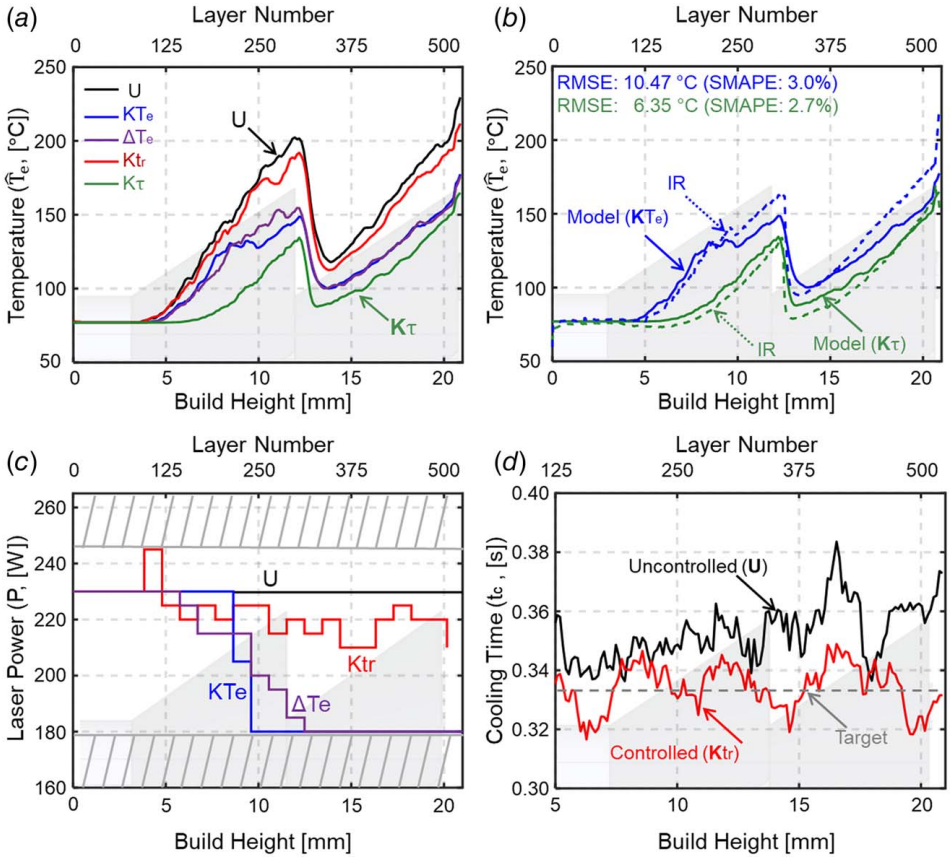

Fig. 18 Model predictive control results for the cone-shaped part. (*a*) Effect of various control strategies on T_e. (*b*) Validation of the KT_e and Kτ strategies with IR thermal imaging data. (*c*) The layerwise change in laser power initiated by the various strategies. (*d*) Effect of Kt_r on the cooling time (target $t_c = 0.335$ s).

Downloaded from http://asmedigitalcollection.asme.org/manufacturingscience/article-pdf/147/8/081005/7500901/manu-25-1025.pdf by Virginia Polytechnic Institute and State University user on 27 June 2025

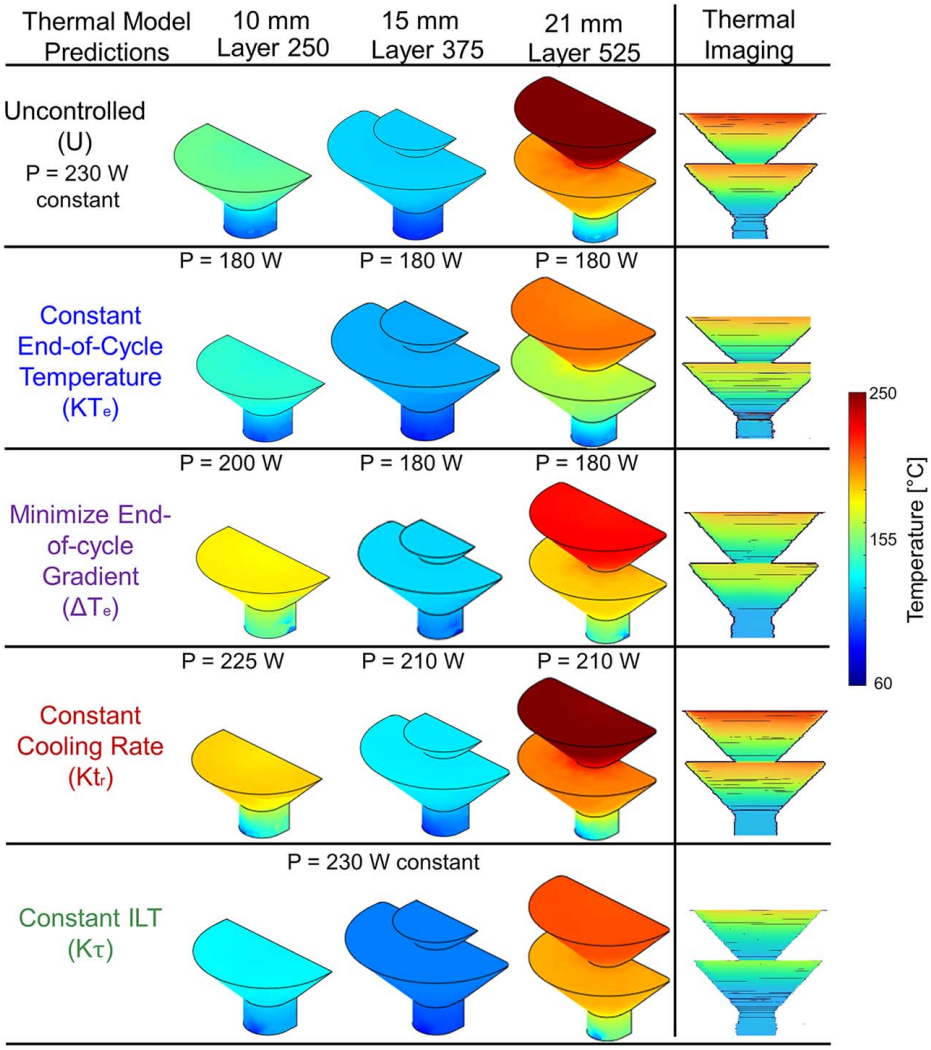

Fig. 19 End-of-cycle temperature ($\hat{T}_e$) predictions for the cone-shaped part with respect to the various thermal control strategies. Shown on the right are the layerwise end-of-cycle temperature measured (T_e) from the IR camera. Note the significant reduction in T_e on account of $\mathbf{K}T_e$, ΔT_e and $\mathbf{K}\tau$ strategies.

In this second build plate, an additional virtual or the so-called ghost part was processed at a laser power of 0 W. The diameter of this fictitious cylindrical-shaped part was varied layer by layer, such that the ILT was $\tau = 57$ s across all layers. The constant $\tau = 57$ s is chosen as it is 1.25× the maximum ILT of 45.6 s observed for the first build plate in Fig. 16.

The advantage of the $\mathbf{K}\tau$ strategy is that it eschews any changes to the processing parameters via the model predictive controller. All processing conditions, apart from the ILT, are maintained identically to the uncontrolled (**U**) case. In other words, $\mathbf{K}\tau$ is not encumbered by the need for thermal simulations, and it is therefore tractable to implement for the practitioner. However, increasing the ILT also increased the build time from 5 h to 8 h. Further, the $\mathbf{K}\tau$ strategy does not account for differences in shape between parts, and presence of features, such as steep overhangs and thin walls. Compared in Fig. 17 are the model-predicted end-of-cycle surface temperature ($\hat{T}_e$) for uncontrolled (**U**) and $\mathbf{K}\tau$ strategies. The latter leads to a significant decrease in $\hat{T}_e$.

5 Results

5.1 Cone (*c*)

5.1.1 Thermal History. Shown in Fig. 18(*a*) are the average end-of-cycle temperature predictions ($\hat{T}_e$) for the five thermal control strategies pertaining to the cone-shaped geometry (*c*). Visual 3D depictions of the thermal history alongside the layerwise composite IR image data are shown in Fig. 19. The end-of-cycle temperature in the descending order of the five scenarios are as follows: **U**, $\mathbf{K}t_r$, $\mathbf{\Delta}T_e$, $\mathbf{K}T_e$, and $\mathbf{K}\tau$. The model predictions for the $\mathbf{K}T_e$ and $\mathbf{K}\tau$ scenarios are validated in Fig. 18(*b*). The model-predicted end-of-cycle temperature $\hat{T}_e$ matches with the IR-measured T_e with SMAPE < 3% (RMSE ~ 10 °C), and the computation time for one iteration was ~4 min.

In Figs. 18(*a*) and 19, significant heat retention is observed in the cone for the first 12 mm of build height. $\hat{T}_e$ increases steadily beginning at 5 mm to the end of 12 mm. It then reduces sharply during the start of the second overhang region, before beginning to increase again. For the uncontrolled scenario (**U**), $\hat{T}_e$ ranges from 125 °C to 200 °C. By contrast, the constant interlayer time ($\mathbf{K}\tau$) thermal history control strategy reduces the range of $\hat{T}_e$ to approximately 100 °C to 150 °C. Due to the progressive variation in the layerwise cross section of the geometry, none of the four thermal history control approaches were able to eliminate the large temperature fluctuations.

The layerwise laser power alterations established by model predictive control for each of the strategies are shown in Fig. 18(*c*). Each of these process parameter recommendations converged within 1.5 h. For the cone-shaped geometry, both the constant end-of-cycle temperature ($\mathbf{K}T_e$) and thermal gradient minimization

Downloaded from http://asmedigitalcollection.asme.org/manufacturingscience/article-pdf/147/8/081005/7500901/manu-25-1025.pdf by Virginia Polytechnic Institute and State University user on 27 June 2025

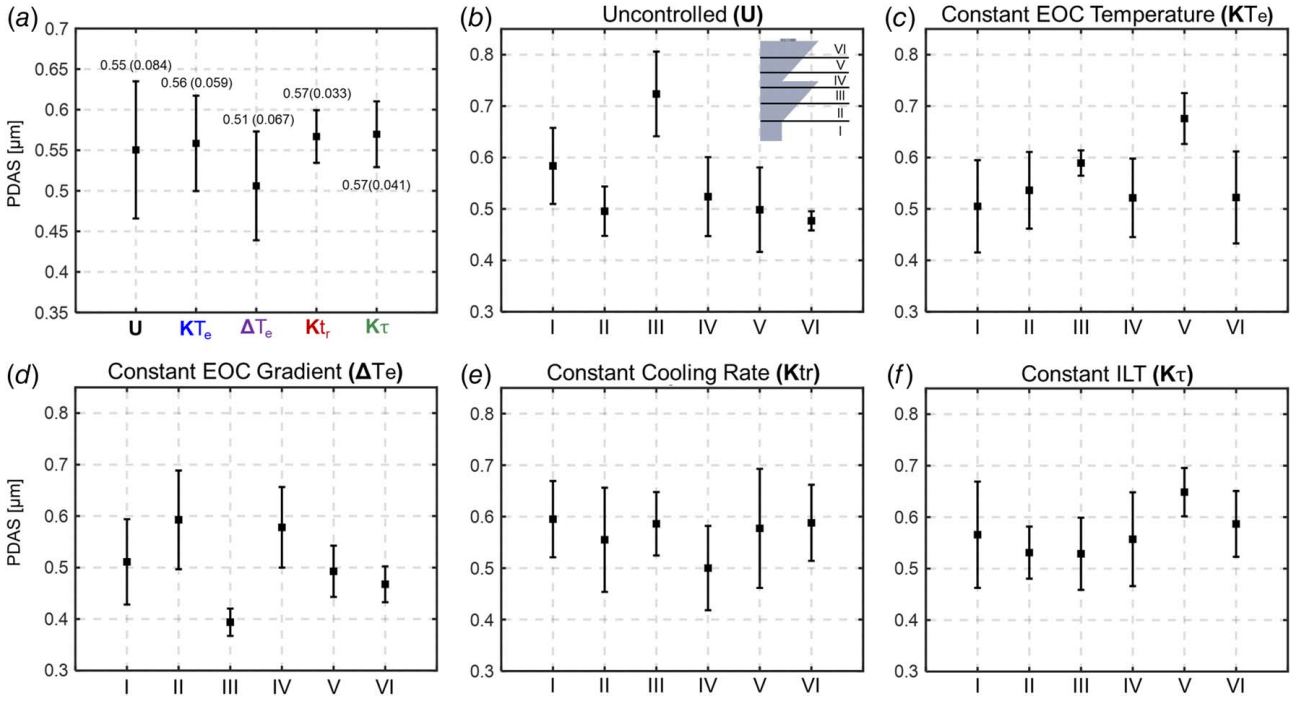

Fig. 20 Comparison of the primary dendritic arm spacing (λ_1) for the cone-shaped part. (*a*) Mean $\lambda_1 \pm 1$ standard deviation in parenthesis as a function of various thermal history scenarios. (*b*)–(*f*) Location-specific PDAS for each of the five scenarios. Control of cooling rate (Kt_c) reduces heterogeneity in grain size.

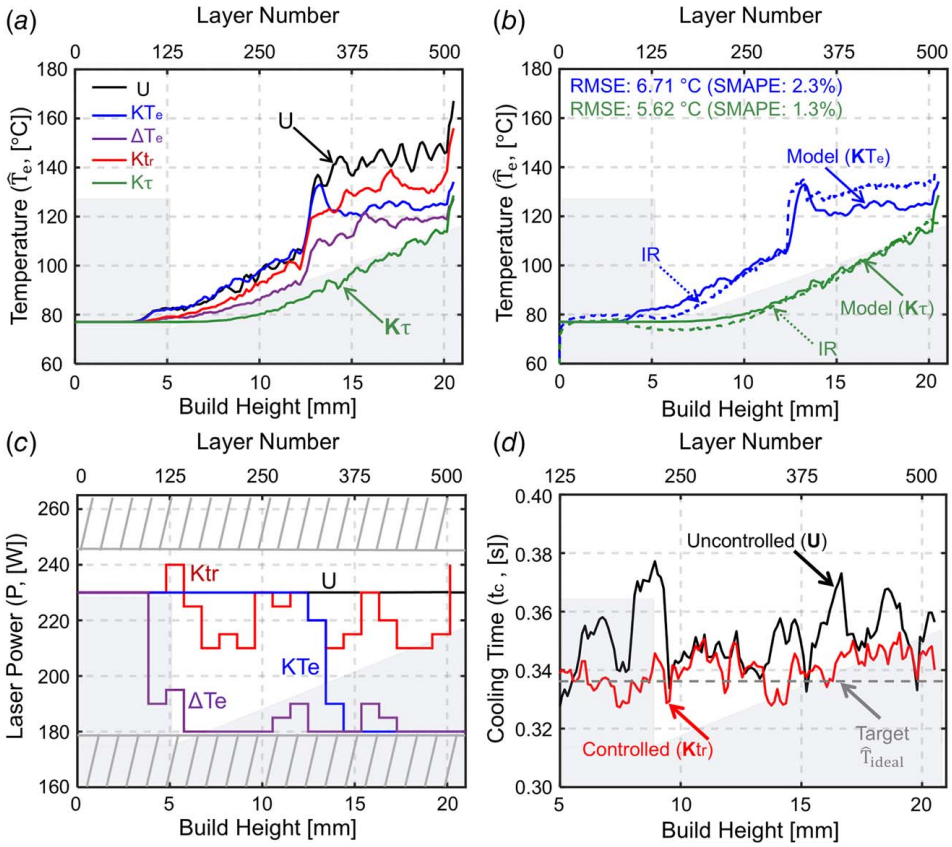

Fig. 21 Model predictive control results for the overhang-shaped part. (*a*) Effect of various control strategies on T_e. (*b*) Validation of the KT_e and Kτ strategies with IR thermal imaging data. (*c*) The layerwise change in laser power initiated by the various strategies. (*d*) Effect of Kt_r on the cooling time (target $t_c = 0.335$ s).

Downloaded from http://asmedigitalcollection.asme.org/manufacturingscience/article-pdf/147/8/081005/7500901/manu-25-1025.pdf by Virginia Polytechnic Institute and State University user on 27 June 2025

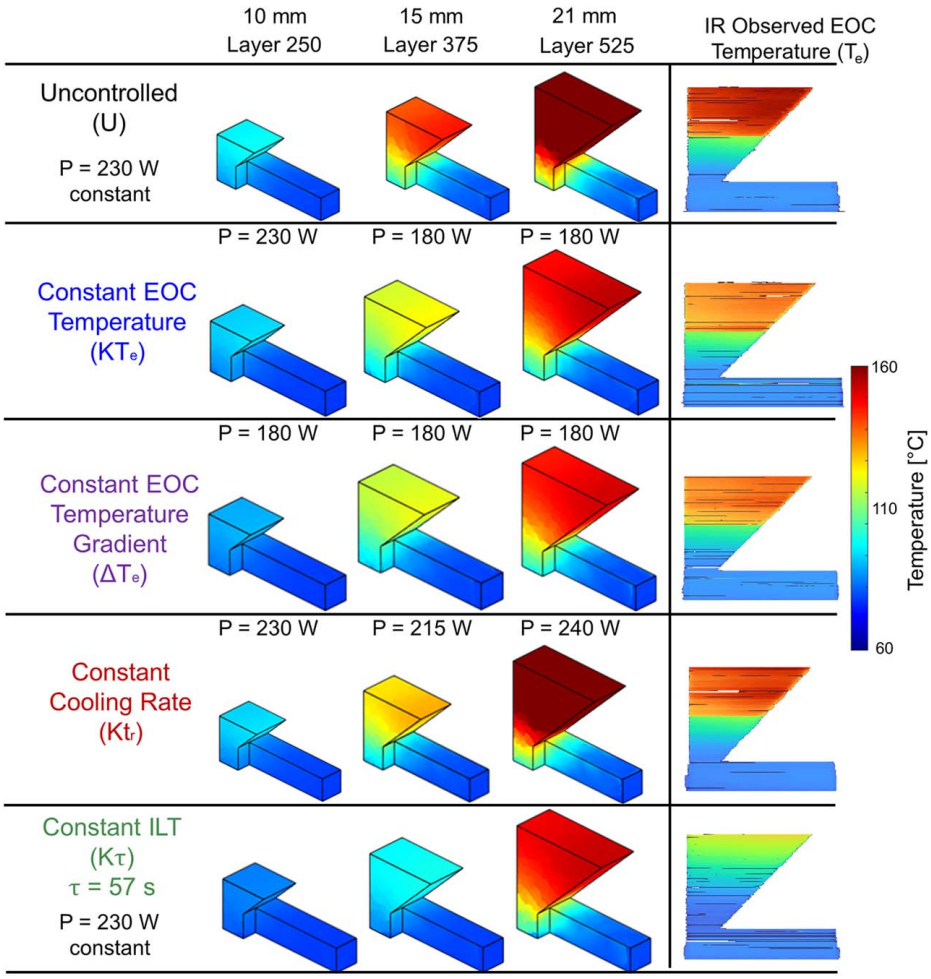

Fig. 22 End-of-cycle temperature ($\hat{T}_e$) predictions for the overhang-shaped part (*S*) for the various thermal control strategies. Shown on the right is the layerwise end-of-cycle temperature measured (T_e) from the IR camera. Note the significant reduction in T_e on account of KT_e, ΔT_e, and Kτ strategies.

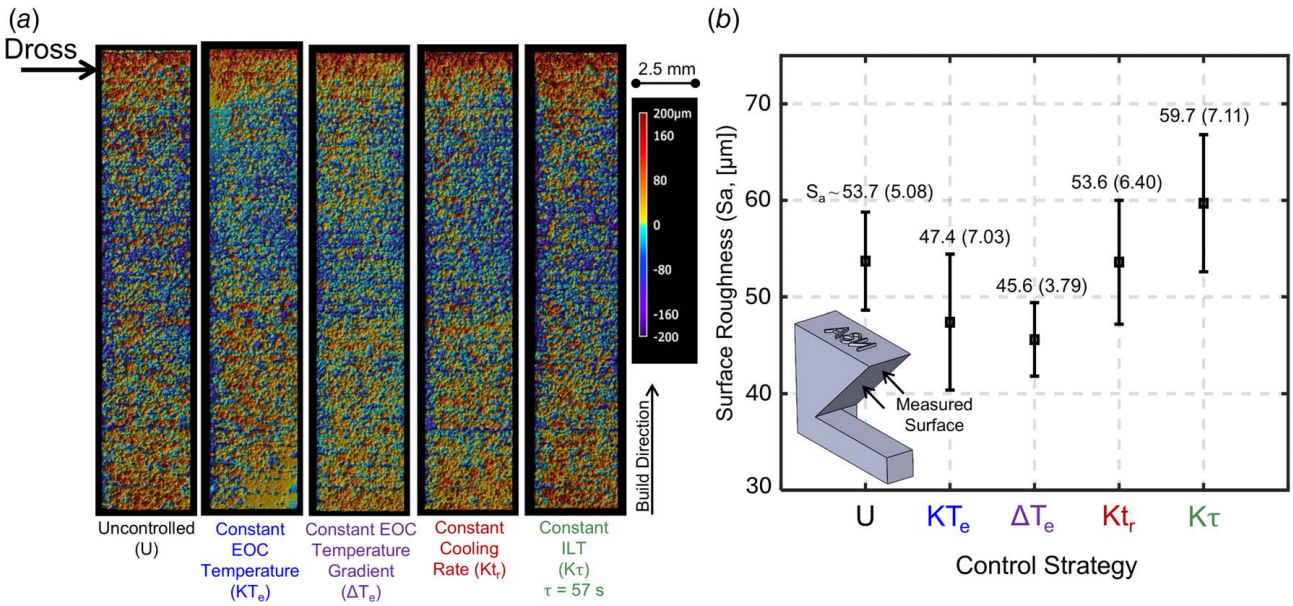

Fig. 23 (*a*) Laser confocal images of the downward-facing surface of the overhang part and (*b*) mean and standard deviation (parentheses) in areal surface finish (Sa) for the five strategies

Downloaded from http://asmedigitalcollection.asme.org/manufacturingscience/article-pdf/147/8/081005/7500901/manu-25-1025.pdf by Virginia Polytechnic Institute and State University user on 27 June 2025

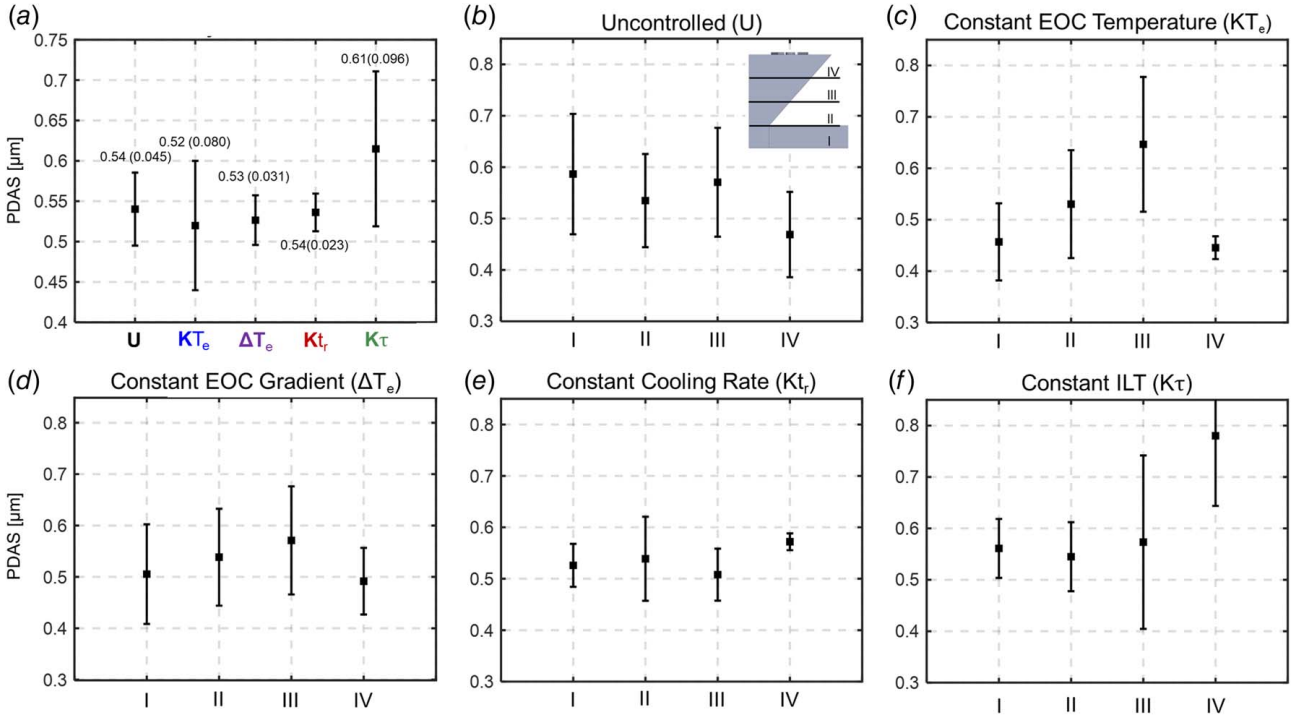

Fig. 24 Comparison of the primary dendritic arm spacing (λ_1). (*a*) Mean $\lambda_1 \pm 1$ standard deviation of $n = 40$ measurements as a function of various thermal history scenarios. (*b*)–(*f*) Location-specific PDAS for each of the five scenarios. Control of cooling rate (Kt_c) reduces heterogeneity in grain size.

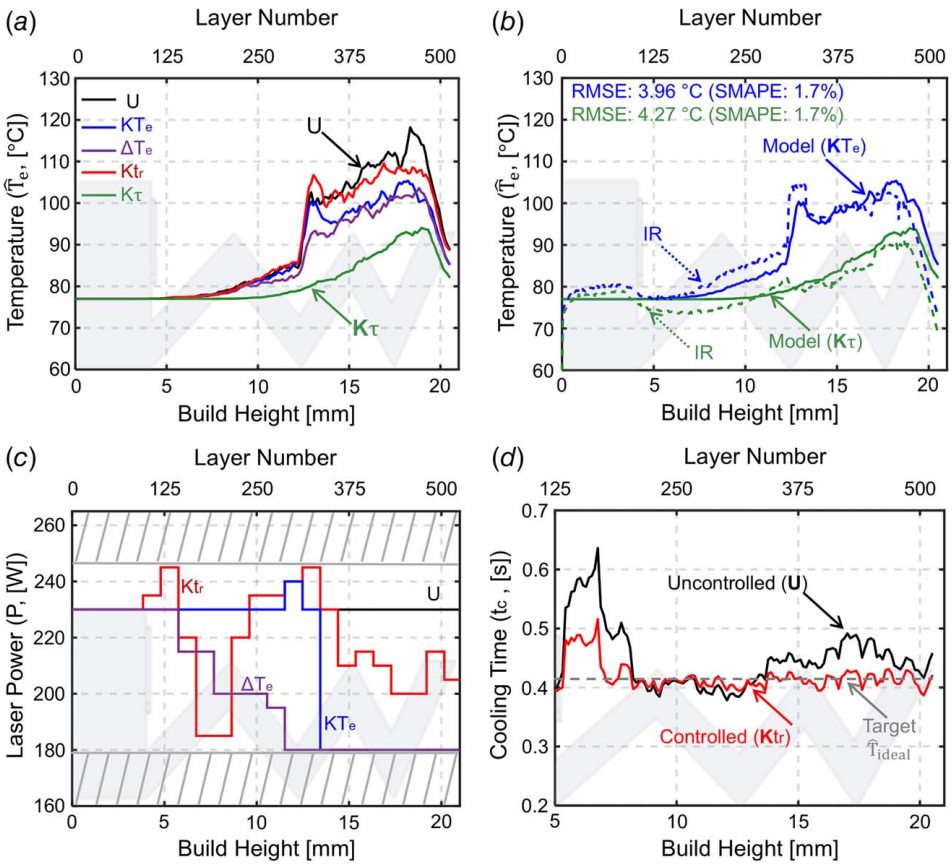

Fig. 25 Model predictive control results for the spring-shaped part. (*a*) Effect of various control strategies on T_e. (*b*) Validation of the KT_e and $K\tau$ strategies with thermal imaging data. (c) The layerwise change in laser power initiated by the various strategies. (*d*) Effect of Kt_r on the cooling time (target $t_c = 0.41$ s).

Downloaded from http://asmedigitalcollection.asme.org/manufacturingscience/article-pdf/147/8/081005/7500901/manu-25-1025.pdf by Virginia Polytechnic Institute and State University user on 27 June 2025

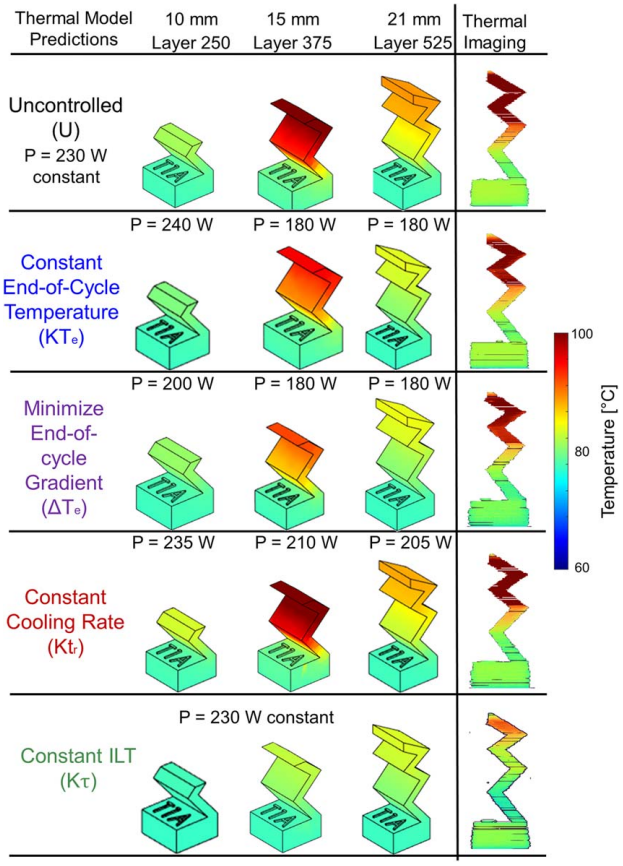

Fig. 26 End-of-cycle temperature ($\hat{T}_e$) predictions for the spring-shaped part (*S*) for the various thermal control strategies. Shown on the right are layerwise end-of-cycle temperature measured from the IR camera. Note the significant reduction in T_e on account of $\mathbf{K}T_e$, ΔT_e, and $\mathbf{K}\tau$ strategies.

($\mathbf{\Delta}T_e$) strategies resulted in similar laser power adjustments and therefore similar end-of-cycle temperature responses. The predicted cooling time (t_c) for $\mathbf{K}t_r$ and **U** are shown in Fig. 18(*d*). For **U**, t_c tends to fluctuate between 0.34 s and 0.38 s, while $\mathbf{K}t_r$ restricts the variation in cooling time $t_c = 0.335 \pm 0.01$ s. The effect of the various control strategies on the grain size (primary dendritic arm spacing) is described in Sec. 5.1.2.

5.1.2 Primary Dendritic Arm Spacing. The PDAS (λ_1) was measured at 12 locations on each of the five cone-shaped parts as detailed in Sec. 3.3.2, Fig. 8(*c*). Figure 20(*a*) quantifies the average and standard deviation of λ_1 across the entire part with respect to the five different thermal history control scenarios. There are 48 PDAS λ_1 readings per part, for a total of 240 measurements. The mean λ_1 is similar for all five scenarios; however, the standard deviations σ_{λ_1} are different. The $\mathbf{K}t_r$ strategy results in the smallest variation, with standard deviation $\sigma_{\lambda_1} = 33$ nm. By contrast, for the uncontrolled scenario (**U**), $\sigma_{\lambda_1} = 84$ nm. Likewise, the rest of the control strategies are significantly consistent, i.e., smaller σ_{λ_1} compared to **U**. The smallest variation in PDAS observed for $\mathbf{K}t_r$ is followed by $\mathbf{K}\tau$ ($\sigma_{\lambda_1} = 41$ nm) and $\mathbf{K}T_e$ ($\sigma_{\lambda_1} = 59$ nm), and $\mathbf{\Delta}T_e$ ($\sigma_{\lambda_1} = 67$ nm). Further, Fig. 20(*b*) presents the mean λ_1 and σ_{λ_1} stratified per region for each of the five parts, affirming the superior consistency in grain size afforded by the $\mathbf{K}t_r$ and $\mathbf{K}\tau$ approaches.

5.2 Overhang (*O*)

5.2.1 Thermal History. Shown in Fig. 21(*a*) are the average end-of-cycle temperature predictions ($\hat{T}_e$) for each of the five scenarios pertaining to the overhang geometry (*O*). Figure 22 depicts 3D renderings of the thermal history at various layers alongside layerwise composite of the end-of-cycle temperature (T_e) acquired from the IR camera.

In Fig. 21(*a*), the end-of-cycle temperature ($\hat{T}_{\text{original}}$) for the uncontrolled scenario (**U**) depicts a sharp increase at 12.5 mm build height, owing to the increase in part surface area and corresponding reduction in the interlayer time (τ) observed in Fig. 16. This observation is further corroborated in Fig. 22. Heat accumulation in **U** is exacerbated in later overhang edges of the part. The largest reduction in average end-of-cycle temperature $\hat{T}_e$ in comparison to $\hat{T}_{\text{original}}$ achieved by the four strategies in the descending order is as follows: $\mathbf{K}\tau$, $\mathbf{\Delta}T_e$, $\mathbf{K}T_e$, and $\mathbf{K}t_r$. These are consistent with the findings for the cone-shaped part. Shown in Fig. 21(*b*) is the model-predicted end-of-cycle temperature ($\hat{T}_e$) for the top layer of the part compared to the T_e measured from the thermal camera for two representative scenarios, $\boldsymbol{KT}_e$, and $\mathbf{K}_\tau$. In both cases, RMSE < 7 °C, and SMAPE < 3%. An iteration of the thermal simulation converged within 1 min.

The layerwise laser power changes implemented for each of the scenarios are depicted in Fig. 21(*c*); each of these was obtained within 21 min. Compared to the other strategies, $\mathbf{\Delta}T_e$ initiates a rapid control response that mitigates the sharp temperature rise anticipated at 12.5 mm. Shown in Fig. 21(*d*) is the effect of implementing $\mathbf{K}t_r$ on cooling time (t_c). The $\mathbf{K}t_r$ strategy mitigates variations in t_c between ± 0.015 s of the target $t_c = 0.335$ s. By contrast for the uncontrolled scenario **U**, t_c ranges from 0.33 s to 0.38 s.

5.2.2 Surface Finish. The surface finish of the downward-facing overhang surface was measured using laser confocal microscopy. As evident from Fig. 23(*a*), partially sintered powder particles, also called dross, were adhered to the downward-facing

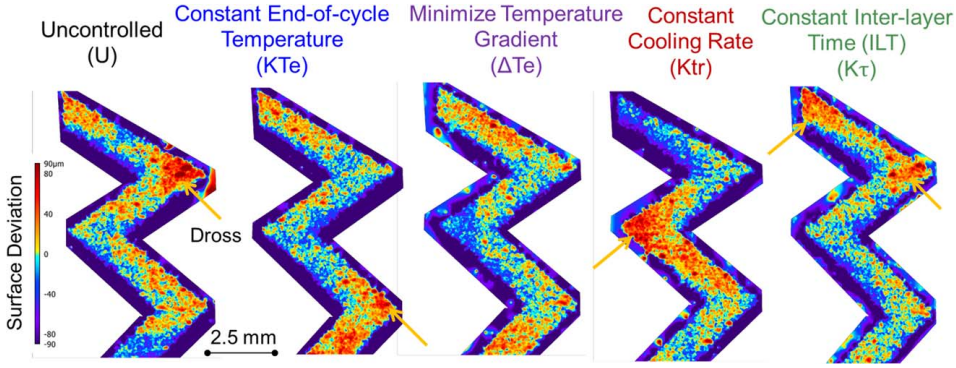

Fig. 27 Confocal microscopy images of the five spring parts created in this work. Severe dross formation was observed in the uncontrolled condition (*U*). Dross formation is mitigated using minimize temperature gradient strategy.

Downloaded from http://asmedigitalcollection.asme.org/manufacturingscience/article-pdf/147/8/081005/7500901/manu-25-1025.pdf by Virginia Polytechnic Institute and State University user on 27 June 2025

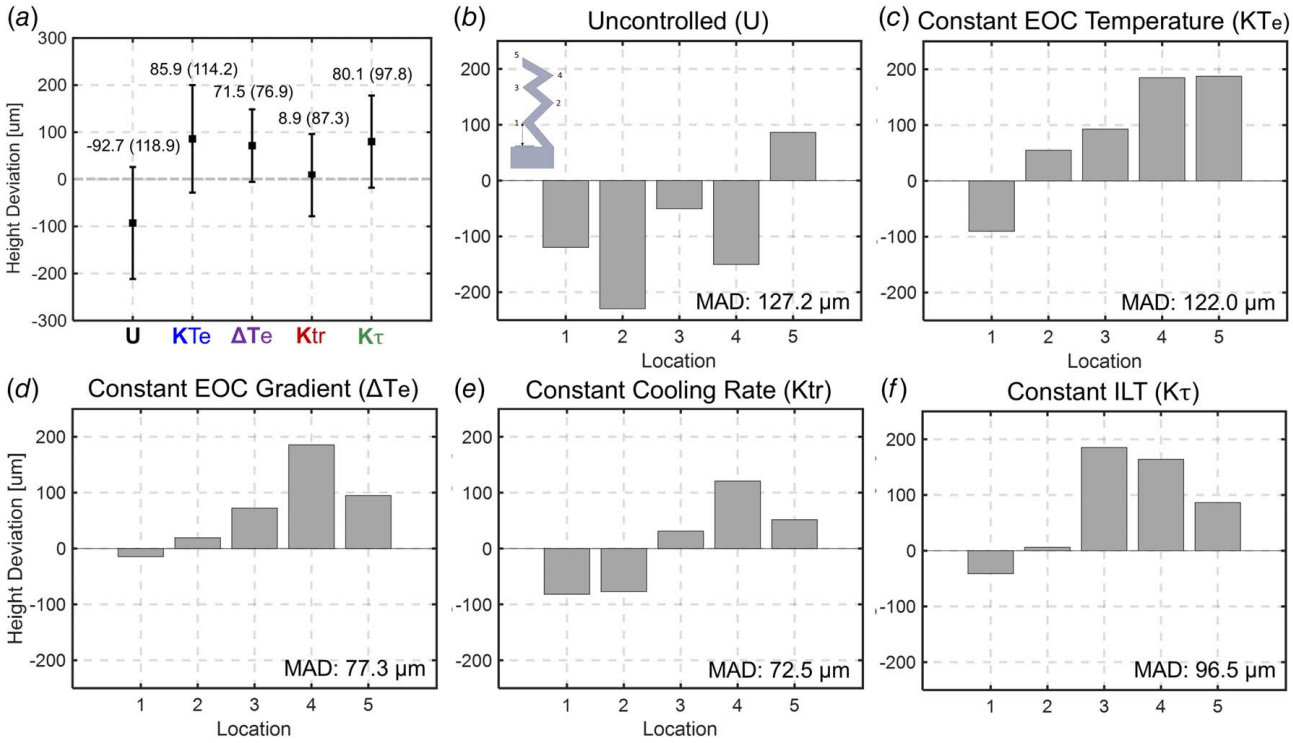

Fig. 28 Assessment of geometric distortion observed in the spring part. (*a*) Overall deviation in height and (*b*)–(*f*) location-specific deviations for each of the five scenarios.

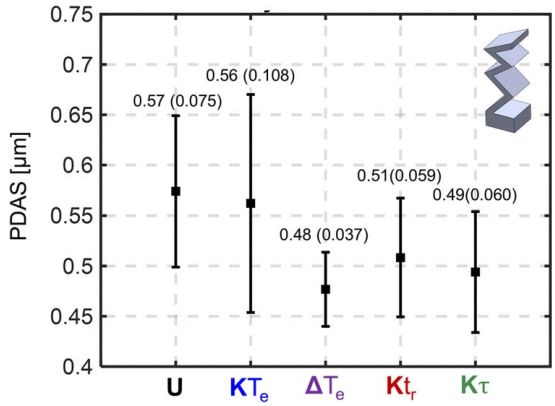

Fig. 29 Comparison of the primary dendritic arm spacing (λ_1) for the various control strategies ($n = 44$ for each thermal control strategy)

surfaces [66]. Dross formation is accorded to heat retention in the overhang region [65]. Comparing Figs. 22 and 23, higher heat retention partially correlates with dross formation. For example, on account of heat retention, dross formation is particularly exacerbated under uncontrolled (**U**) processing and constant cooling rate ($\mathbf{K}t_r$). The reduced heat retention of the constant end-of-cycle temperature ($\mathbf{K}T_e$) and minimal thermal gradient ($\mathbf{\Delta}T_e$) strategies mitigate dross formation.

The least average areal surface roughness (Sa) is observed for $\mathbf{\Delta}T_e$ and $\mathbf{K}T_e$ strategies, and for these scenarios, Sa ~ 45 μm and 47 μm, respectively. The $\mathbf{\Delta}T_e$ approach results in the smallest standard deviation $\sigma_{Sa} \sim 3.8$ μm. By contrast, for the uncontrolled (**U**) case, Sa ~ 53 μm with $\sigma_{Sa} \sim 5$ μm. Notably, dross formation and surface finish are exacerbated for $\mathbf{K}\tau$ despite having the least degree of heat retention. This is explained based on the findings of Charles et al. [65,66]. The authors observed that dross formation is a function of heat retention at the part-level and behavior of the meltpool. At high volumetric energy density, Charles et al. [65] noted that the meltpool enters keyhole mode near the vicinity of the overhang surface. In the $\mathbf{K}\tau$ strategy, while the part-level end-of-cycle temperature T_e is mitigated, the laser power is maintained at a constant level of 230 W, i.e., the same value of the uncontrolled (**U**) condition. Hence, the tendency to enter keyhole mode at the boundary remains elevated in the $\mathbf{K}\tau$ strategy.

5.2.3 Primary Dendritic Arm Spacing. PDAS (λ_1) was measured in ten locations on each of the five overhang parts as detailed in Sec. 3.3.2, Fig. 8. The average and standard deviation of the layerwise PDAS measurements are reported in Fig. 24(*a*); 40 λ_1 readings were acquired per part, for a total of 200 measurements. While the average $\lambda_1 \approx 525$ nm was similar for all strategies (except $\mathbf{K}\tau$), the standard deviation (σ_{λ_1}) was different. $\mathbf{K}t_r$ and $\mathbf{\Delta}T_e$ strategies resulted in $\sigma_{\lambda_1} = 23$ nm and 31 nm, respectively, compared to $\sigma_{\lambda_1} \sim 45$ nm for **U**. However, $\mathbf{K}T_e$ and $\mathbf{K}\tau$ strategies underperform for this case.

Shown in Figs. 24(*b*)–24(*f*) are the PDAS measurements at each of the four layerwise sections. At these representative locations, $\mathbf{\Delta}T_e$ and $\mathbf{K}t_r$ control strategies result in a more consistent and smaller grain sizes compared to the other scenarios. These results indicate that the cooling rate is a critical determinant of microstructure evolution consistent with observations for a similar part in our previous work [30].

5.3 Spring (*s*)

5.3.1 Thermal History. Shown in Fig. 25(*a*) are the end-of-cycle temperature ($\hat{T}_e$) predictions for the spring (S) under various thermal history control scenarios. The predicted $\hat{T}_e$ is rendered in 3D in Fig. 26, along with the layerwise end-of-cycle temperature (T_e) measured using the IR camera.

As evident from Figs. 25(*a*) and 26, the uncontrolled spring part (**U**) tends to retain heat at approximately 12.5 mm build height, especially in the overhang region. Compared to **U**, $\mathbf{K}T_e$, $\mathbf{\Delta}T_e$, and

Downloaded from http://asmedigitalcollection.asme.org/manufacturingscience/article-pdf/147/8/081005/7500901/manu-25-1025.pdf by Virginia Polytechnic Institute and State University user on 27 June 2025

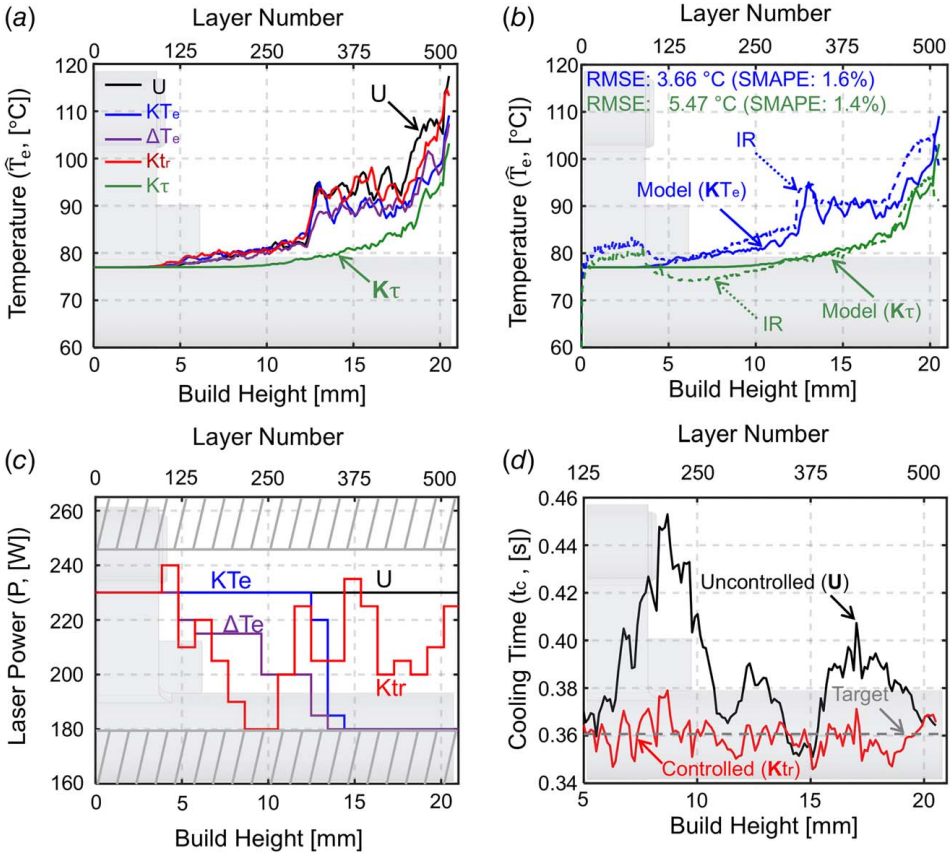

Fig. 30 Model predictive control results for the bell crank part. (*a*) Effect of various control strategies on T_e. (*b*) Validation of the KT_e and Kτ strategies with IR thermal imaging data. (c) The layerwise change in laser power initiated by the various strategies. (*d*) Effect of Kt_r on the cooling time (target $t_c = 0.335$ s).

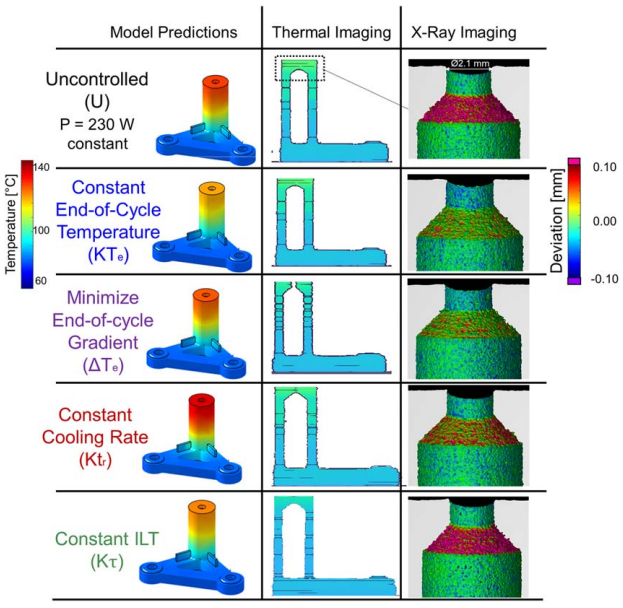

Fig. 31 (Left) End-of-cycle temperature ($\hat{T}_e$) predictions for the bell crank-shaped part (*B*) with respect to the various thermal control strategies. (Center) Layerwise end-of-cycle temperature measured (T_e) from the IR camera. (Right) Geometric deviations within the internal cavity measured using X-ray CT scans (CAD compare).

Kτ control strategies significantly reduce the peak $\hat{T}_e$. The Kt_r strategy does not prominently reduce T_e as it aims to control the cooling time (t_c) and not T_e. The thermal model predictions for KT_e and Kτ are validated with experimental data shown in Fig. 25(*b*). For all cases, RMSE < 5 °C and SMAPE < 4%, and a single iteration converged within 7 min.

The layerwise laser power adjustments initiated by the various strategies are compared in Fig. 25(*c*). An entire run of the model predictive control strategy for the spring-shaped part typically required 2.5 h. The effect of Kt_r on t_c is shown in Fig. 25(*d*). The target $t_c = 0.41$ s. A sharp increase in t_c is observed at approximately 6 mm and 12.5 mm build height due to the corresponding decrease in interlayer time. The former rise was only partially mitigated due to the lower bound on the laser power (182 W). The latter rise at 12.5 mm was largely eliminated by model predictive control.

5.3.2 Surface Integrity. The surface integrity and geometric accuracy of the spring-shaped part were assessed using laser confocal microscopy. As evident from Fig. 27, dross formation is observed for downward-facing overhang surfaces of the spring-shaped part. Comparing Figs. 26 and 27, higher heat retention generally exacerbates dross formation. Consistent with prior observations for the overhang geometry (*O*), discussed in Sec. 5.2.2, dross formation is excessive under uncontrolled (**U**) processing and Kt_r strategies. The ΔT_e strategy and to a lesser extent KT_e and Kτ strategies mitigate dross formation. We note that the relatively complex nature of the spring-shaped part impedes access to the underside of the overhang for measurement of surface finish.

Downloaded from http://asmedigitalcollection.asme.org/manufacturingscience/article-pdf/147/8/081005/7500901/manu-25-1025.pdf by Virginia Polytechnic Institute and State University user on 27 June 2025

5.3.3 Geometric Accuracy. Geometric accuracy was measured at five points labeled 1–5 according to the method described in Sec. 3.3.1, Fig. 8. Shown in Fig. 28(*a*) is the mean deviation from the design for each of the thermal history control strategies. The $\mathbf{K}t_r$ strategy has the least mean deviation from the design. While all five parts depict peak deviation in the range of 100–200 μm, the $\mathbf{K}t_r$ strategy has a mean deviation of approximately zero, with the smallest standard deviation (90 μm).

The location-wise deviations for the various strategies are presented in Figs. 28(*b*)–28(*f*). Positive deviation indicates that the distance measured was larger than the nominal design. For the uncontrolled case (**U**), Fig. 28(*b*) depicts the largest MAD of 127 μm. The MAD for **U** is negative as the excessive melting of powder resulted in oversize downward-facing sections and hence smaller distance from the base. The smallest MAD of 72 μm is reported for $\mathbf{K}t_r$, followed by $\mathbf{\Delta}T_e$ (MAD ~ 77 μm), $\mathbf{K}\tau$ (MAD ~ 96 μm), and $\mathbf{K}T_e$ (MAD ~ 122 μm).

5.3.4 Primary Dendritic Arm Spacing. Figure 29 quantifies the average and standard deviation of PDAS (λ_1) for the entire spring-shaped part with respect to the five different scenarios. There are 44 λ_1 readings per part, for a total of 220 measurements across all 5 parts. The within-part variation in grain size was significantly impacted by the choice of control strategy. Consistent with the prior results for the overhang, the $\mathbf{\Delta}T_e$ strategy resulted in mean $\lambda_1 = 480$ nm and the smallest standard deviation in PDAS, $\sigma_{\lambda_1} = 37$ nm. By contrast, for the uncontrolled scenario (**U**), the mean $\lambda_1 = 570$ nm, $\sigma_{\lambda_1} = 75$ nm. $\mathbf{K}t_r$ and $\mathbf{K}\tau$ scenarios provide similar results with mean $\lambda_1 \sim 500$ nm $\sigma_{\lambda_1} < 60$ nm.

5.4 Bell Crank (*B*)

5.4.1 Thermal History. Shown in Fig. 30 are the average end-of-cycle temperature predictions ($\hat{T}_e$) for the five thermal control strategies pertaining to the bell crank geometries (*B*). Shown in Fig. 31 are 3D renderings of the temperature distribution at the final layer and layerwise IR camera data. The end-of-cycle temperatures in the descending order of the five scenarios are as follows: **U**, $\mathbf{K}t_r$, $\mathbf{\Delta}T_e$, $\mathbf{K}T_e$, and $\mathbf{K}\tau$, consistent with prior results for the cone, overhang, and spring geometries. The model predictions for the $\mathbf{K}T_e$ and $\mathbf{K}\tau$ scenarios are validated in Fig. 30(*b*). The model-predicted end-of-cycle temperature $\hat{T}_e$ matches with the IR-measured T_e with SMAPE < 2% and RMSE < 6 °C.

Significant heat accumulation was observed in the last 12 mm of the build height as shown in Fig. 30(*a*). For the uncontrolled scenario, the temperature ranged from 76 °C to 120 °C. By contrast, the $\mathbf{K}\tau$ strategy reduced the peak end-of-cycle temperature to 100 °C. However, no thermal control approach was able to eliminate heat retention in the cylindrical shaft. The layerwise laser power alterations identified by model predictive control for each of the strategies are shown in Fig. 30(*c*). These converged within 3.5 h. For the bell crank geometry, both $\mathbf{K}T_e$ and $\mathbf{\Delta}T_e$ strategies resulted in similar laser power adjustments, which leads to similar end-of-cycle temperature responses. The predicted cooling time (t_c) for $\mathbf{K}t_r$ and **U** is shown in Fig. 30(*d*). t_c fluctuates between 0.35 and 0.45 s for **U**, while $\mathbf{K}t_r$ restricts t_c within ± 0.02 s of the setpoint $t_c = 0.36$ s.

5.4.2 Internal Surface Measurement. Shown in Fig. 31 are the thermal history simulation results for the last layer of the bell crank, consolidated IR images, and cross sections of the internal cavity in the shaft section. Consistent with the observations of Fig. 30(*a*), the uncontrolled (**U**) and $\mathbf{K}t_r$ scenarios depict heat retention in the latter layers of the shaft. The CAD compare feature in VOLUME GRAPHICS software was used to analyze the X-ray CT images. This analysis maps the observed deviation of the overhang feature from the CAD design.

Due to excessive heat retention and dross formation, the internal overhang region of the uncontrolled (**U**) scenario deviates as much as 0.1 mm. The powder trapped within the cavity of the bell crank partially melts and adheres to regions of high heat retention. These findings are similar to dross formation observed in the spring and overhang geometries in Figs. 23 and 27, respectively. The reduced heat retention in the $\mathbf{K}T_e$ and $\mathbf{\Delta}T_e$ control strategies mitigates dross formation and results in improved surface integrity and geometric accuracy. The $\mathbf{K}t_r$ strategy also reduces dross formation, albeit to a lesser degree than $\mathbf{K}T_e$ and $\mathbf{\Delta}T_e$. Consistent with prior results, the constant laser power maintained in the $\mathbf{K}\tau$ strategy fails to inhibit dross formation.

6 Conclusions and Future Works

We developed and applied a physics-based model predictive control approach to regulate the thermal history of LPBF-processed parts. The approach autonomously optimizes the laser power in a layerwise manner such that the thermal history of a part matches an a priori determined ideal thermal trend. We demonstrate through various stainless steel 316L geometries that the appropriate physics-guided process control strategy reduces within-part variation in grain size, enhances geometric accuracy, and improves surface integrity. The approach can thus curtail the need for extensive trial-and-error empirical testing to achieve desired part properties. Specific outcomes from this work are as follows.

(1) The model predictive control strategy was applied to four types of shapes: cone, overhang, spring, and bell crank. These geometries involved challenging-to-print features, such as severe external overhangs, varying overhangs, large layerwise change in cross section, and internal overhangs.
(2) The approach uses a rapid and meshless graph theory-based computational model to autonomously optimize the laser power and thereby control the thermal history before a part is printed—a form of digital feedforward control. The model predictions were validated with in situ infrared thermal imaging data.
(3) Four different thermal history control strategies were tested, namely, (i) maintaining constant end-of-cycle temperature ($\mathbf{K}T_e$); (ii) minimizing the spatial thermal gradients between layers ($\mathbf{\Delta}T_e$); (iii) maintaining a constant cooling rate ($\mathbf{K}t_r$); and (iv) maintaining a constant time between layers ($\mathbf{K}\tau$). In addition, parts were built with uncontrolled (**U**) processing conditions. A total of 20 parts were thus analyzed (=4 part geometries × 5 thermal history control strategies).
(4) The grain size (primary dendritic arm spacing) of samples was characterized postprocess using scanning electron microscopy. The surface finish and geometric integrity were assessed with confocal microscopy. X-ray computed tomography was used for examining internal surfaces of the bell crank.
(5) The $\mathbf{K}t_r$ and $\mathbf{\Delta}T_e$ thermal history control strategies significantly reduced within-part variation in grain size in terms of the primary dendritic arm spacing, as well as mitigated geometric deviation. $\mathbf{\Delta}T_e$ and $\mathbf{K}T_e$ strategies were effective for inhibiting dross formation and thereby improving the surface finish of downward-facing (overhang) surfaces, as well as internal features. The $\mathbf{K}\tau$ approach resulted in a significant reduction in grain size variation in all but the overhang geometry. Thus, the type of thermal control strategy to be employed is contingent on the desired part characteristics.

In future works, we will endeavor to ascertain the effect of thermal history control on part properties, such as hardness and tensile strength.

Acknowledgment

The authors thank the two anonymous reviewers and the associate editor Prof. Arif Malik for their time and diligence. Prahalada

Downloaded from http://asmedigitalcollection.asme.org/manufacturingscience/article-pdf/147/8/081005/7500901/manu-25-1025.pdf by Virginia Polytechnic Institute and State University user on 27 June 2025

Rao acknowledges funding from the National Science Foundation (NSF) via Grant Nos. CMMI-2309483/1752069, OIA-1929172, PFI-TT 2322322/2044710, CMMI-1920245, ECCS-2020246, CMMI-1739696, CMMI-2336449, and CMMI-2428305; US Department of Navy, Naval Surface Warfare Center (NAVAIR, N6833524C0215) and Office of Naval Research (ONR, N00014-21-1-2781); and the National Institute of Standards and Technology (NIST, 70NANB23H029T) for supporting his research program. The characterization aspects of this work were made possible by the use of Virginia Tech's Materials Characterization Facility, which was supported by the Institute for Critical Technology and Applied Science, the Macromolecules Innovation Institute, and the Office of the Vice President for Research and Innovation.

- Understanding the causal influence of process parameters and thermal history on part quality was the major aspect of CMMI-2309483/1752069 (Program Officer: Pranav Soman).
- Commercialization of the graph theory thermal approach for ultrafast simulation of metal additive manufacturing processes is being pursued under PFI-TT 2322322/2044710 (Program Officer: Samir Iqbal). The foregoing two NSF grants partially supported the Ph.D. works of Dr. Alex Riensche, Dr. Ben Bevans, Mr. Mihir Darji, and Mr. Antonio Carrington, Jr.
- Improving part quality in laser powder bed fusion using physics-guided process control was funded via NIST 70NANB23H029T. This grant was currently supporting the Ph.D. studies of Mr. Mihir Darji and Mr. Antonio Carrington.
- Assessment of LPBF part quality and microstructures as a function of processing parameters was funded by N00014-21-1-2781. This grant funded Mr. Kaustubh Deshmukh's Ph.D. work.
- Further improvements to the graph theory thermal modeling approach are being pursued through CMMI-2428305 and CMMI-2336449.

Conflict of Interest

There are no conflicts of interest.

Data Availability Statement

The datasets generated and supporting the findings of this article are obtainable from the corresponding author upon reasonable request.

References

[1] Snyder, J. C., and Thole, K. A., 2020, "Understanding Laser Powder Bed Fusion Surface Roughness," ASME J. Manuf. Sci. Eng., **142**(7), p. 071003.

[2] DebRoy, T., Wei, H. L., Zuback, J. S., Mukherjee, T., Elmer, J. W., Milewski, J. O., Beese, A. M., Wilson-Heid, A., De, A., and Zhang, W., 2018, "Additive Manufacturing of Metallic Components—Process, Structure and Properties," Prog. Mater. Sci., **92**, pp. 112–224.

[3] Sames, W. J., List, F. A., Pannala, S., Dehoff, R. R., and Babu, S. S., 2016, "The Metallurgy and Processing Science of Metal Additive Manufacturing," Int. Mater. Rev., **61**(5), pp. 315–360.

[4] Das, S., Bourell, D. L., and Babu, S. S., 2016, "Metallic Materials for 3D Printing," MRS Bull., **41**(10), pp. 729–741.

[5] Blakey-Milner, B., Gradl, P., Snedden, G., Brooks, M., Pitot, J., Lopez, E., Leary, M., Berto, F., and du Plessis, A., 2021, "Metal Additive Manufacturing in Aerospace: A Review," Mater. Des., **209**, p. 110008.

[6] Najmon, J. C., Raeisi, S., and Tovar, A., 2019, "2—Review of Additive Manufacturing Technologies and Applications in the Aerospace Industry," *Additive Manufacturing for the Aerospace Industry*, F. Froes, and R. Boyer, eds., Elsevier, New York, pp. 7–31.

[7] Kerstens, F., Cervone, A., and Gradl, P., 2021, "End to End Process Evaluation for Additively Manufactured Liquid Rocket Engine Thrust Chambers," Acta Astronaut., **182**, pp. 454–465.

[8] Whitt, A., David, E., and Grandl, P., 2023, "The GRCop story: The Development, Production and Additive Manufacturing of NASA's Rocket Engine Alloys," https://www.metal-am.com/articles/the-grcop-storythe-development-production-and-additive-manufacturing-of-nasas-rocket-engine-alloys/, Accessed June 24, 2024.

[9] Mcmahon, M., 2023, "Metal AM in the Aerospace Sector: From Early Successes to the Transformation of an Industry," https://www.metal-am.com/articles/metal-am-in-the-aerospace-sector-from-early-successes-to-the-transformation-of-an-industry/, Accessed June 24, 2024.

[10] Seifi, M., Gorelik, M., Waller, J., Hrabe, N., Shamsaei, N., Daniewicz, S., and Lewandowski, J. J., 2017, "Progress Towards Metal Additive Manufacturing Standardization to Support Qualification and Certification," JOM, **69**(3), pp. 439–455.

[11] Gradl, P. R., Tinker, D. C., Ivester, J., Skinner, S. W., Teasley, T., and Bili, J. L., 2021, "Geometric Feature Reproducibility for Laser Powder Bed Fusion (L-PBF) Additive Manufacturing With Inconel 718," Addit. Manuf., **47**, p. 102305.

[12] Shahwaz, M., Nath, P., and Sen, I., 2022, "A Critical Review on the Microstructure and Mechanical Properties Correlation of Additively Manufactured Nickel-Based Superalloys," J. Alloys Compd., **907**, p. 164530.

[13] Chowdhury, S., Yadaiah, N., Prakash, C., Ramakrishna, S., Dixit, S., Gupta, L. R., and Buddhi, D., 2022, "Laser Powder Bed Fusion: A State-of-the-Art Review of the Technology, Materials, Properties & Defects, and Numerical Modelling," J. Mater. Res. Technol., **20**, pp. 2109–2172.

[14] Mostafaei, A., Zhao, C., He, Y., Ghiaasiaan, S. R., Shi, B., Shao, S., Shamsaei, N., et al., 2022, "Defects and Anomalies in Powder Bed Fusion Metal Additive Manufacturing," Curr. Opin. Solid State Mater. Sci., **26**(2), p. 100974.

[15] Snow, Z., Nassar, A. R., and Reutzel, E. W., 2020, "Invited Review Article: Review of the Formation and Impact of Flaws in Powder Bed Fusion Additive Manufacturing," Addit. Manuf., **36**, p. 101457.

[16] Spears, T. G., and Gold, S. A., 2016, "In-Process Sensing in Selective Laser Melting (SLM) Additive Manufacturing," Integr. Mater. Manuf. Innov., **5**(1), pp. 16–40.

[17] Gor, M., Soni, H., Wankhede, V., Sahlot, P., Grzelak, K., Szachgluchowicz, I., and Kluczyński, J., 2021, "A Critical Review on Effect of Process Parameters on Mechanical and Microstructural Properties of Powder-Bed Fusion Additive Manufacturing of SS316L," Materials, **14**(21), p. 6527.

[18] Yavari, R., Smoqi, Z., Riensche, A., Bevans, B., Kobir, H., Mendoza, H., Song, H., Cole, K., and Rao, P., 2021, "Part-Scale Thermal Simulation of Laser Powder Bed Fusion Using Graph Theory: Effect of Thermal History on Porosity, Microstructure Evolution, and Recoater Crash," Mater. Des., **204**, p. 109685.

[19] Jensen, S. C., Carroll, J. D., Pathare, P. R., Saiz, D. J., Pegues, J. W., Boyce, B. L., Jared, B. H., and Heiden, M. J., 2023, "Long-Term Process Stability in Additive Manufacturing," Addit. Manuf., **61**, p. 103284.

[20] Sanchez, S., Smith, P., Xu, Z., Gaspard, G., Hyde, C. J., Wits, W. W., Ashcroft, I. A., Chen, H., and Clare, A. T., 2021, "Powder Bed Fusion of Nickel-Based Superalloys: A Review," Int. J. Mach. Tools Manuf., **165**, p. 103729.

[21] Chen, Z., Han, C., Gao, M., Kandukuri, S. Y., and Zhou, K., 2022, "A Review on Qualification and Certification for Metal Additive Manufacturing," Virtual Phys. Prototyp., **17**(2), pp. 382–405.

[22] Mostafaei, A., Ghiaasiaan, R., Ho, I. T., Strayer, S., Chang, K.-C., Shamsaei, N., Shao, S., et al., 2023, "Additive Manufacturing of Nickel-Based Superalloys: A State-of-the-Art Review on Process-Structure-Defect-Property Relationship," Prog. Mater. Sci., **136**, p. 101108.

[23] Haferkamp, L., Haudenschild, L., Spierings, A., Wegener, K., Riener, K., Ziegelmeier, S., and Leichtfried, G. J., 2021, "The Influence of Particle Shape, Powder Flowability, and Powder Layer Density on Part Density in Laser Powder Bed Fusion," Metals, **11**(3), p. 418.

[24] Mohr, G., Altenburg, S. J., and Hilgenberg, K., 2023, "On the Limitations of Small Cubes as Test Coupons for Process Parameter Optimization in Laser Powder Bed Fusion of Metals," J. Laser Appl., **35**(4), p. 042029.

[25] Frazier, W. E., 2014, "Metal Additive Manufacturing: A Review," J. Mater. Eng. Perform., **23**(6), pp. 1917–1928.

[26] Foteinopoulos, P., Papacharalampopoulos, A., and Stavropoulos, P., 2018, "On Thermal Modeling of Additive Manufacturing Processes," CIRP J. Manuf. Sci. Technol., **20**, pp. 66–83.

[27] Williams, R. J., Piglione, A., Rønneberg, T., Jones, C., Pham, M.-S., Davies, C. M., and Hooper, P. A., 2019, "In Situ Thermography for Laser Powder Bed Fusion: Effects of Layer Temperature on Porosity, Microstructure and Mechanical Properties," Addit. Manuf., **30**, p. 100880.

[28] Qin, Y., Lou, S., Shi, P., Qi, Q., Zeng, W., Scott, P. J., and Jiang, X., 2024, "Optimisation of Process Parameters for Improving Surface Quality in Laser Powder Bed Fusion," Int. J. Adv. Manuf. Technol., **130**(5), pp. 2833–2845.

[29] Du, B., Liu, Q., He, M., Yi, J., He, J., and Wang, S., 2023, "The Heterogeneous Microstructure in Laser Powder Bed Fabricated Inconel 718 Pillar and Its Influence on Mechanical Properties," Mater. Sci. Eng. A, **872**, p. 144953.

[30] Riensche, A. R., Bevans, B. D., King, G., Krishnan, A., Cole, K. D., and Rao, P., 2024, "Predicting Meltpool Depth and Primary Dendritic Arm Spacing in Laser Powder Bed Fusion Additive Manufacturing Using Physics-Based Machine Learning," Mater. Des., **237**, p. 112540.

[31] Mayne, D. Q., 2014, "Model Predictive Control: Recent Developments and Future Promise," Automatica, **50**(12), pp. 2967–2986.

[32] Schwenzer, M., Ay, M., Bergs, T., and Abel, D., 2021, "Review on Model Predictive Control: An Engineering Perspective," Int. J. Adv. Manuf. Technol., **117**(5–6), pp. 1327–1349.

[33] Cole, K. D., Riensche, A., and Rao, P. K., 2022, "Discrete Green's Functions and Spectral Graph Theory for Computationally Efficient Thermal Modeling," Int. J. Heat Mass Transfer, **183**, p. 122112.

[34] Druzgalski, C. L., Ashby, A., Guss, G., King, W. E., Roehling, T. T., and Matthews, M. J., 2020, "Process Optimization of Complex Geometries Using Feed Forward Control for Laser Powder Bed Fusion Additive Manufacturing," Addit. Manuf., **34**, p. 101169.

Downloaded from http://asmedigitalcollection.asme.org/manufacturingscience/article-pdf/147/8/081005/7500901/manu-25-1025.pdf by Virginia Polytechnic Institute and State University user on 27 June 2025

[35] King, W., 2023, "Process Control for Defect Mitigation in Laser Powder Bed Fusion Additive Manufacturing," SAE Research Report EPR2023011.
[36] Yavari, R., Riensche, A., Tekerek, E., Jacquemetton, L., Halliday, H., Vandever, M., Tenequer, A., et al., 2021, "Digitally Twinned Additive Manufacturing: Detecting Flaws in Laser Powder Bed Fusion by Combining Thermal Simulations With In-Situ Meltpool Sensor Data," Mater. Des., **211**, p. 110167.
[37] Smoqi, Z., Gaikwad, A., Bevans, B., Kobir, M. H., Craig, J., Abul-Haj, A., Peralta, A., and Rao, P., 2022, "Monitoring and Prediction of Porosity in Laser Powder Bed Fusion Using Physics-Informed Meltpool Signatures and Machine Learning," J. Mater. Process. Technol., **304**, p. 117550.
[38] Bandyopadhyay, A., and Traxel, K. D., 2018, "Invited Review Article: Metal-Additive Manufacturing—Modeling Strategies for Application-Optimized Designs," Addit. Manuf., **22**, pp. 758–774.
[39] Luo, Z., and Zhao, Y., 2018, "A Survey of Finite Element Analysis of Temperature and Thermal Stress Fields in Powder Bed Fusion Additive Manufacturing," Addit. Manuf., **21**, pp. 318–332.
[40] Sarkar, D., Kapil, A., and Sharma, A., 2024, "Advances in Computational Modeling for Laser Powder Bed Fusion Additive Manufacturing: A Comprehensive Review of Finite Element Techniques and Strategies," Addit. Manuf., **85**, p. 104157.
[41] Riensche, A., Bevans, B. D., Smoqi, Z., Yavari, R., Krishnan, A., Gilligan, J., Piercy, N., Cole, K., and Rao, P., 2022, "Feedforward Control of Thermal History in Laser Powder Bed Fusion: Toward Physics-Based Optimization of Processing Parameters," Mater. Des., **224**, p. 111351.
[42] Peter, N., Pitts, Z., Thompson, S., and Saharan, A., 2020, "Benchmarking Build Simulation Software for Laser Powder Bed Fusion of Metals," Addit. Manuf., **36**, p. 101531.
[43] Bevans, B., Barrett, C., Spears, T., Gaikwad, A., Riensche, A., Smoqi, Z., Halliday, H., and Rao, P., 2023, "Heterogeneous Sensor Data Fusion for Multiscale, Shape Agnostic Flaw Detection in Laser Powder Bed Fusion Additive Manufacturing," Virtual Phys. Prototyp., **18**(1), p. e2196266.
[44] Imani, F., Gaikwad, A., Montazeri, M., Rao, P., Yang, H., and Reutzel, E., 2018, "Process Mapping and In-Process Monitoring of Porosity in Laser Powder Bed Fusion Using Layerwise Optical Imaging," ASME J. Manuf. Sci. Eng., **140**(10), p. 101009.
[45] Riensche, A., Bevans, B., Carrington, A., Deshmukh, K., Shephard, K., Sions, J., Synder, K., Plotnikov, Y., Cole, K., and Rao, P., 2025, "DynamicPrint: A Physics-Guided Feedforward Model Predictive Process Control Approach for Defect Mitigation in Laser Powder Bed Fusion Additive Manufacturing," Addit. Manuf., **97**, p. 104592.
[46] Fang, Q., Xiong, G., Zhou, M., Tamir, T. S., Yan, C. B., Wu, H., Shen, Z., and Wang, F. Y., 2024, "Process Monitoring, Diagnosis and Control of Additive Manufacturing," IEEE Trans. Autom. Sci. Eng., **21**(1), pp. 1041–1067.
[47] Bolton, W., 2002, "1—Control Systems," *Control Systems*, W. Bolton, ed., Newnes, Oxford, pp. 1–36.
[48] Dodds, S. J., 2015, *Feedback Control*, Vol. 10, Springer, London, pp. 978–971.
[49] Wang, R., Standfield, B., Dou, C., Law, A. C., and Kong, Z. J., 2023, "Real-Time Process Monitoring and Closed-Loop Control on Laser Power via a Customized Laser Powder Bed Fusion Platform," Addit. Manuf., **66**, p. 103449.
[50] Renken, V., Lübbert, L., Blom, H., von Freyberg, A., and Fischer, A., 2018, "Model Assisted Closed-Loop Control Strategy for Selective Laser Melting," Procedia CIRP, **74**, pp. 659–663.
[51] Vasileska, E., Demir, A. G., Colosimo, B. M., and Previtali, B., 2022, "A Novel Paradigm for Feedback Control in LPBF: Layer-Wise Correction for Overhang Structures," Adv. Manuf., **10**(2), pp. 326–344.
[52] Kavas, B., Balta, E. C., Tucker, M., Rupenyan, A., Lygeros, J., and Bambach, M., 2023, "Layer-to-Layer Closed-Loop Feedback Control Application for Inter-Layer Temperature Stabilization in Laser Powder Bed Fusion," Addit. Manuf., **78**, p. 103847.
[53] Adnan, M., Yang, H. C., Kuo, T. H., Cheng, F. T., and Tran, H. C., 2021, "MPI-Based System 2 for Determining LPBF Process Control Thresholds and Parameters," IEEE Robot. Autom. Lett., **6**(4), pp. 6553–6560.
[54] Mahmoud, D., Magolon, M., Boer, J., Elbestawi, M. A., and Mohammadi, M. G., 2021, "Applications of Machine Learning in Process Monitoring and Controls of L-PBF Additive Manufacturing A Review," Appl. Sci., **11**(24), p. 11910.
[55] McCann, R., Obeidi, M. A., Hughes, C., McCarthy, É, Egan, D. S., Vijayaraghavan, R. K., Joshi, A. M., et al., 2021, "In-Situ Sensing, Process Monitoring and Machine Control in Laser Powder Bed Fusion: A Review," Addit. Manuf., **45**, p. 102058.
[56] Yagmur, A., Paakkonen, I., and Miles, A., 2023, "The Hitchhiker's Guide to Smart Fusion," https://www.eos.info/en-us/innovations/smart-fusion, Accessed July 25, 2024.
[57] Yeung, H., Lane, B., and Fox, J., 2019, "Part Geometry and Conduction-Based Laser Power Control for Powder Bed Fusion Additive Manufacturing," Addit. Manuf., **30**, p. 100844.
[58] He, C., Ramani, K. S., and Okwudire, C. E., 2023, "An Intelligent Scanning Strategy (SmartScan) for Improved Part Quality in Multi-Laser PBF Additive Manufacturing," Addit. Manuf., **64**, p. 103427.
[59] Ramani, K. S., He, C., Tsai, Y.-L., Okwudire, C. E., and Malekipour, E., 2022, "SmartScan: An Intelligent Scanning Approach for Uniform Thermal Distribution, Reduced Residual Stresses and Deformations in PBF Additive Manufacturing," Addit. Manuf., **52**, p. 102643.
[60] Wang, Q., Michaleris, P., Nassar, A. R., Irwin, J. E., Ren, Y., and Stutzman, C. B., 2020, "Model-Based Feedforward Control of Laser Powder Bed Fusion Additive Manufacturing," Addit. Manuf., **31**, p. 100985.
[61] Ogoke, F., and Farimani, A. B., 2021, "Thermal Control of Laser Powder Bed Fusion Using Deep Reinforcement Learning," Addit. Manuf., **46**, p. 102033.
[62] Kusano, M., and Watanabe, M., 2024, "Controlling Heat Accumulation Through Changing Time per Layer in Laser Powder Bed Fusion of Nickel-Based Superalloy," J. Manuf. Processes, **131**, pp. 187–198.
[63] Deshmukh, K., Riensche, A., Bevans, B., Lane, R. J., Snyder, K., Halliday, H., Williams, C. B., Mirzaeifar, R., and Rao, P., 2024, "Effect of Processing Parameters and Thermal History on Microstructure Evolution and Functional Properties in Laser Powder Bed Fusion of 316L," Mater. Des., **244**, p. 113136.
[64] Reza Yavari, M., Williams, R. J., Cole, K. D., Hooper, P. A., and Rao, P., 2020, "Thermal Modeling in Metal Additive Manufacturing Using Graph Theory: Experimental Validation With Laser Powder Bed Fusion Using In Situ Infrared Thermography Data," ASME J. Manuf. Sci. Eng., **142**(12), p. 121005.
[65] Charles, A., Bayat, M., Elkaseer, A., Thijs, L., Hattel, J. H., and Scholz, S., 2022, "Elucidation of Dross Formation in Laser Powder Bed Fusion at Down-Facing Surfaces: Phenomenon-Oriented Multiphysics Simulation and Experimental Validation," Addit. Manuf., **50**, p. 102551.
[66] Charles, A., Elkaseer, A., Paggi, U., Thijs, L., Hagenmeyer, V., and Scholz, S., 2021, "Down-Facing Surfaces in Laser Powder Bed Fusion of Ti6Al4V: Effect of Dross Formation on Dimensional Accuracy and Surface Texture," Addit. Manuf., **46**, p. 102148.
[67] Krakhmalev, P., Fredriksson, G., Svensson, K., Yadroitsev, I., Yadroitsava, I., Thuvander, M., and Peng, R., 2018, "Microstructure, Solidification Texture, and Thermal Stability of 316 L Stainless Steel Manufactured by Laser Powder Bed Fusion," Metals, **8**(8), p. 643.
[68] Zhang, H., Li, C., Guo, Q., Ma, Z., Li, H., and Liu, Y., 2019, "Improving Creep Resistance of Nickel-Based Superalloy Inconel 718 by Tailoring Gamma Double Prime Variants," Scr. Mater., **164**, pp. 66–70.
[69] Watring, D. S., Benzing, J. T., Hrabe, N., and Spear, A. D., 2020, "Effects of Laser-Energy Density and Build Orientation on the Structure–Property Relationships in As-Built Inconel 718 Manufactured by Laser Powder Bed Fusion," Addit. Manuf., **36**, p. 101425.
[70] Schoinochoritis, B., Chantzis, D., and Salonitis, K., 2015, "Simulation of Metallic Powder Bed Additive Manufacturing Processes With the Finite Element Method: A Critical Review," Proc. Inst. Mech. Eng. B, **231**(1), pp. 96–117.
[71] Yavari, M. R., Cole, K. D., and Rao, P., 2019, "Thermal Modeling in Metal Additive Manufacturing Using Graph Theory," ASME J. Manuf. Sci. Eng., **141**(7), p. 071007.
[72] Cole, K. D., Yavari, M. R., and Rao, P. K., 2020, "Computational Heat Transfer with Spectral Graph Theory: Quantitative Verification," Int. J. Therm. Sci., **153**, p. 106383.
[73] Ye, J., Khairallah, S. A., Rubenchik, A. M., Crumb, M. F., Guss, G., Belak, J., and Matthews, M. J., 2019, "Energy Coupling Mechanisms and Scaling Behavior Associated With Laser Powder Bed Fusion Additive Manufacturing," Adv. Eng. Mater., **21**(7), p. 1900185.
[74] Zhai, W., Wu, N., and Zhou, W., 2022, "Effect of Interpass Temperature on Wire Arc Additive Manufacturing Using High-Strength Metal-Cored Wire," Metals, **12**(2), p. 212.
[75] Wang, Q., Michaleris, P., Pantano, M., Li, C., Ren, Y., and Nassar, A. R., 2022, "Part-Scale Thermal Evolution and Post-Process Distortion of Inconel-718 Builds Fabricated by Laser Powder Bed Fusion," J. Manuf. Processes, **81**, pp. 865–880.
[76] Kobir, M. H., Yavari, R., Riensche, A. R., Bevans, B. D., Castro, L., Cole, K. D., and Rao, P., 2023, "Prediction of Recoater Crash in Laser Powder Bed Fusion Additive Manufacturing Using Graph Theory Thermomechanical Modeling," Prog. Addit. Manuf., **8**(3), pp. 355–380.
[77] Vecchiato, F. L., de Winton, H., Hooper, P. A., and Wenman, M. R., 2020, "Melt Pool Microstructure and Morphology From Single Exposures in Laser Powder Bed Fusion of 316L Stainless Steel," Addit. Manuf., **36**, p. 101401.

Downloaded from http://asmedigitalcollection.asme.org/manufacturingscience/article-pdf/147/8/081005/7500901/manu-25-1025.pdf by Virginia Polytechnic Institute and State University user on 27 June 2025